Metabolic pathways fuelling Devil Facial Tumour Disease

Anne-Lise Gérard[1,*], Florence Pirard[1,2], Caitlin Vanbeek[1], Antoine M. Dujon[1,2], Aaron G. Schultz[1], Rodrigo Hamede[3], Hannah V. Siddle[4], Frédéric Thomas[2], Matthew McKenzie[1,5], Mark Ziemann[1,6], Beata Ujvari[1,*]

[1] School of Life and Environmental Sciences, Deakin University, Waurn Ponds, Victoria, 3218, Australia
[2] Centre for Ecological and Evolutionary Cancer Research, MIVEGEC, University of Montpellier, CNRS, IRD, Montpellier, Occitania, 34090, France
[3] School of Natural Sciences, University of Tasmania, Hobart, Tasmania, 7000, Australia
[4] Queensland Alliance for Agriculture & Food Innovation, The University of Queensland, Brisbane, Queensland, 4072, Australia
[5] Institute for Physical Activity and Nutrition, Deakin University, Waurn Ponds, Victoria, 3218, Australia
[6] Burnet Institute, Melbourne, Victoria, 3004, Australia

Corresponding authors: Beata Ujvari (beata.ujvari@deakin.edu.au), Anne-Lise Gérard (anne-lise.gerard@evobio.eu).

RUNNING TITLE
Metabolic Drivers of Devil Facial Tumours

ABBREVIATIONS

2DG — 2-deoxy-D-glucose

2DG6P — 2-deoxyglucose-6-phosphate

ADO — 2-aminoethanethiol dioxygenase

ACSL1/3/4 — acyl-CoA synthetase long-chain family member 1/3/4

AIC — Akaike's Information Criterion

AKT — protein kinase B

ATP — adenosine triphosphate

BTN — bivalve transmissible neoplasia

CO□ — carbon dioxide

CPT1A — carnitine palmitoyltransferase 1A

dNTP — deoxyribonucleotide triphosphate

DEG(s) — differentially expressed gene(s)

DFT — Devil Facial Tumour

DFT1 — Devil Facial Tumour 1

DFT2 — Devil Facial Tumour 2

DFTD — Devil Facial Tumour Disease(s)

DNA — deoxyribonucleic acid

ETC — electron transport chain

FBS — fetal bovine serum

FDR — false discovery rate

FSHR — follicle-stimulating hormone receptor

g — relative centrifugal force (×g)

GSH — glutathione

H2DCFDA — 2′,7′-dichlorodihydrofluorescein diacetate

HK3 — hexokinase 3

HKDC1 — hexokinase domain containing 1

kb — kilobase

MDS — multidimensional scaling

MHC — major histocompatibility complex

mRNA — messenger ribonucleic acid

MTT — 3-(4,5-dimethylthiazol-2-yl)-2,5-diphenyltetrazolium bromide

NADPH — nicotinamide adenine dinucleotide phosphate (reduced form)

OXPHOS — oxidative phosphorylation

PCR — polymerase chain reaction

PDGF — platelet-derived growth factor

PDGFRA — platelet-derived growth factor receptor alpha

PFKM — phosphofructokinase, muscle-type

PI3K — phosphoinositide 3-kinase

PPP — pentose phosphate pathway

RFU — relative fluorescence units

RIN — RNA Integrity Number

RNA — ribonucleic acid

ROS — reactive oxygen species

RPM — revolutions per minute

TCA — tricarboxylic acid (cycle)

µM / mM — micromolar / millimolar

KEYWORDS
Cancer, Transcriptomics, Pathway Enrichment, Glycolysis, Reactive Oxygen Species, Cholesterol Biosynthesis

CONFLICTS OF INTEREST
The authors declare no conflicts of interest.

ABSTRACT

Devil Facial Tumour Diseases (DFTD), threatening Tasmanian devils, consist of two distinct transmissible cancers, DFT1 and DFT2, with differing origins and geographic spread. We investigated the metabolic differences between DFT1 and DFT2, examining cell viability, metabolic outputs, and bulk gene expression. Using both DFT1 and DFT2 cell lines and biopsies, we found that glycolysis, oxidative phosphorylation, glutamate metabolism and fatty acid synthesis are all essential for the survival of both tumour types. However, DFT2 exhibited higher rates of glycolysis and lactate generation compared to DFT1. This coincided with elevated ATP production, cholesterol biosynthesis and ROS generation, as well as an increased reliance on fatty acid metabolism. Furthermore, DFT2 is less metabolically adaptable than DFT1, being unable to switch to oxidative phosphorylation as DFT1 can when required. These metabolic changes in DFT2, in conjunction with its higher growth rate, suggests a more aggressive cancer phenotype than DFT1. Our findings highlight distinct metabolic adaptations in DFT2 that may contribute to its competitive advantage.

INTRODUCTION

In multicellular organisms, cell division is tightly regulated to maintain tissue integrity and function. Such regulatory mechanisms comprise, but are not limited to, cell cycle checkpoints [1], telomere length [2] and immunosurveillance [3]. When one or several of these safeguards are impaired, cells proliferate uncontrollably, which can lead to cancer. Traits tumour cells acquire on the path to becoming cancerous are known as the hallmarks of cancer [4, 5]. One important hallmark is the deregulation of cellular metabolism, as tumour cells need to generate the necessary resources (nucleotides, building blocks for membranes, electron acceptors, etc.) to sustain high cell division rates. Cancer cells also evolve in a challenging environment where oxygen and nutrient availability vary over space and time with tumour size and vascularisation. Hence these cells must rewire their metabolism to produce enough precursors and energy, while also maintaining redox homeostasis by detoxifying excess reactive oxygen species (ROS) produced by the mitochondria [6].

The most common metabolic alteration found in cancer cells is increased glucose uptake and fermentation of glucose to lactate, also known as the “Warburg effect” [7]. Whilst normal cells completely oxidise glucose through the tricarboxylic acid (TCA) cycle and the electron transport chain (ETC; i.e., oxidative phosphorylation or OXPHOS), cancer cells convert most glucose to lactate through aerobic glycolysis [7]. The Warburg effect allows cancer cells to produce energy in the form of adenosine triphosphate (ATP) along with reducing equivalents at a higher rate compared to OXPHOS. Moreover, aerobic glycolysis has been shown to: (i) promote tissue invasion and immune evasion, (ii) drive the biosynthesis of nucleotides, lipids, and proteins, and finally (iii) play a role in cell signalling through ROS and chromatin modulation[8]. Alternatively, glucose can enter the pentose phosphate pathway (PPP) and participate in nucleotide synthesis. The PPP is also a major source of nicotinamide adenine dinucleotide phosphate (NADPH), contributing to ROS detoxification [7].

Aside from glucose, other molecules fuel cancer metabolism with glutamine being the second most consumed nutrient by cancer cells [7]. Most glutamine is converted to glutamate which can then be further processed to amino acids, nucleotides, or α-ketoglutarate, respectively contributing to protein synthesis, nucleic acid production and fuelling the TCA cycle [7, 9, 10]. Furthermore, cancer cells harness lipid metabolism to obtain sufficient energy (ATP), building blocks for their membranes, and signalling molecules for proliferation, survival, invasion, and metastasis [11]. Precursors and products of the TCA cycle such as glucose, acetyl coenzyme A (acetyl-CoA) and citrate can be used to produce lipids including fatty acids and cholesterol [7, 9]. Both enhanced lipid synthesis and lipid breakdown have been linked to cancer development [7].

These metabolic alterations occur not only during cancer development but also throughout the metastatic cascade (i.e., when cells detach from the extracellular matrix, travel through the bloodstream, and establish in a new tissue) [6]. An even more radical environmental change occurs in transmissible cancers where cancer cells are passed on from one individual to another as allo- or xeno-grafts [12–14]. Only two studies have investigated metabolic changes

in transmissible cancers, one in bivalve transmissible neoplasia (BTN) [15] that impacts a variety of shellfish species and the other in Devil Facial Tumour 1 (DFT1) [16] that is endangering Tasmanian devils [17, 18]. The study on BTN used transcriptomics to identify key cancer drivers in bivalve neoplastic cells and found many metabolic pathways (including TCA and glycolysis) to be altered in BTN cells compared to healthy haemolymph cells [15]. The study on DFT1 used a more focused, assay-based approach and found that DFT1 depends on carbohydrate metabolism to proliferate [16]. DFT1 has resulted in 60% of population loss [19] and resulted in the species being listed as endangered on the IUCN Red List.

Devil Facial Tumour Diseases (DFTD) are two transmissible facial cancers affecting the Tasmanian devil (*Sarcophilus harrisii*) [14]. The diseases are fatal and passed on through biting, which is frequent during social interactions [20]. DFTD consist of two distinct cancers that arose independently in separate founder animals: DFT1, estimated to have emerged in 1986 in Northeast Tasmania, and DFT2, estimated to have emerged in 2011 in the Southeast of the island [14, 21, 22]. Both cancers cause facial tumours that eventually lead to animals dying from starvation or organ failure due to metastatic disease within six to twelve months after the appearance of visible tumours [21, 23, 24]. Although both cancers cause similar clinical symptoms, a few notable differences between them exist that include (i) devil- and cell type-of-origin, (ii) geographical spread and (iii) *in vitro* growth dynamics. First, DFT1 originated from a myelinating Schwann cell of a female devil, while DFT2 originated from an immature or repair Schwann cell of a male devil [25, 26]. Interestingly, repair Schwann cells show increased motility and proliferation compared to differentiated Schwann cells [27], potentially translating to more aggressive cancers prone to metastasise. Second, DFT1 has propagated to most of Tasmania while DFT2 has a restricted geographic range, only recently affecting devils outside of the peninsula where it originated to co-occur with DFT1 [28]. This has led to three reported cases of co-infection with both DFT1 and DFT2 in devils, and competition between the two diseases for hosts has been hypothesised [29]. In a recent *in vitro* study, DFT1 cells were observed to grow slower in comparison to DFT2 cells, with DFT2 outcompeting DFT1 in co-cultures [30].

Recent work by Gérard et al.[30] hypothesised that differences in DFT1 and DFT2 growth dynamics could be explained by the distinct differentiation state of their Schwann cell-of-origin [26]. For instance, less differentiated repair Schwann cells dramatically increase glycolysis to assist in peripheral nerve repair [27]. This should translate into metabolic differences ultimately responsible for DFT1 and DFT2's diverging *in vitro* growth dynamics and competitiveness.

Here, we investigate similarities and differences between DFT1 and DFT2 metabolism by growing cell lines in the presence of metabolic inhibitors and measuring cell viability. We also measured outputs of major metabolic pathways such as cholesterol content, lactate, ATP, and ROS production. To link our functional assays to gene expression data, we generated full transcriptomes for DFT1 and DFT2 cell lines and reanalysed previously published transcriptomes from tumour biopsies taken from wild infected animals [26]. We highlight

distinct metabolic adaptations in DFT2 that may underpin its increased proliferative capacity and competitive advantage over DFT1.

Though rare, transmissible cancers offer real-world insight into cancer survival under stress as they exhibit extreme metabolic flexibility, mirroring human cancers during metastasis and therapy resistance. Understanding their metabolic vulnerabilities could position DFTD cells as natural models for testing inhibitors and identifying biomarkers for aggressive or treatment-resistant cancers. Investigating them can reveal how tumours evolve and adapt metabolically, providing a unique window into cancer biology.

RESULTS

Many enriched pathways are shared between DFT cell lines and biopsies

To understand the metabolic differences between DFT1 and DFT2, we used bulk RNA-sequencing of DFT1 and DFT2 cell cultures and tumour biopsies. According to multidimensional scaling (MDS), tumour biopsies clustered into distinct groups, suggesting clear differences between DFT1 and DFT2 (Fig 1A). DFT1 and DFT2 cell lines also separated into two distinct clusters on the first dimension of the MDS plots (Fig. 1B). When combining both datasets, cell lines clustered separately from tumour biopsies on the first dimension, and DFT1 cell lines grouped away from DFT2 cell lines on the second dimension (Fig. 1C). Interestingly, the biopsies did not cluster according to DFT on the second dimension, indicating less variability between DFT1 and DFT2 biopsies than between DFT1 and DFT2 cell line gene expression profiles. Thus, DFT biopsies were more similar in gene expression than DFT cell lines. Biopsy tumour purity was comparable to cell line tumour purity (78.77% and 79.34% respectively; Table S1), indicating minimal contamination with healthy host tissue.

Differential gene expression analysis revealed nearly twice as many DEGs between DFT1 and DFT2 cell lines compared to biopsies (8,612 DEGs and 4,569 DEGs, respectively). Cell lines show 4,200 up-regulated and 4,412 down-regulated genes in DFT2 compared to DFT1, while biopsies show 2,536 up-regulated and 2,033 down-regulated genes. Overall, more genes were detected in the cell lines than in the biopsies (17,468 and 15,931). Heatmaps of the top 20 up- and down-regulated genes, ranked by log fold-change (logFC) show cell lines and biopsies clustering by DFT (Fig. 1D). This grouping is less striking for the DFT2 biopsies, where 13 of the top 20 upregulated genes are solely overexpressed in one of the two samples. The most upregulated gene in DFT2 cell lines was *PDGFRA*, a receptor for platelet derived growth factors, and the most downregulated one was *NTS*, which may be involved in the regulation of fat metabolism [54]. In DFT2 biopsies, these genes are *SMTNL1* and *UBE2M*, respectively (see Table S2 for a full list of gene symbols, names, and brief descriptions). However, these genes are solely differentially expressed in one of the two biopsy samples.
Of the genes differentially expressed in both cell lines and biopsies, it was found that RFX4 and HOXD13, both of which encode transcription factors, and TNR, whose product is a neural extracellular matrix protein, were upregulated in both DFT2 cell lines and biopsies. Three genes, *CHRNA3*, *CLDN19* and *SSX2IP* were present within the top 20 downregulated genes in DFT2, both in cell lines and biopsies. CHRNA3 plays a role in neurotransmission, CLDN19 in tight junctions between cells and SSX2IP in eliminating ROS.

To understand pathway-level gene expression patterns, a multi-contrast enrichment analysis revealed 178 significantly enriched gene sets, i.e., sets with coordinated up or coordinated down regulation of genes (FDR < 0.05; Fig. 1E; Fig. S1). Most sets (153) showed concordant enrichment between cell line and biopsy data (top-right and bottom-left quadrants in Fig. 1E).

From these, 145 were upregulated in both DFT2 cell lines and biopsies and 8 were downregulated. Conversely, 25 significantly enriched gene sets showed discordant enrichment between cell lines and biopsies. Overall, although DFT cell lines diverge more in terms of gene expression than DFT biopsies, a vast majority of significantly enriched pathways are shared between both datasets.

Gene sets expected (or known) to be differentially expressed between DFT2 and DFT1 were concordantly upregulated in our analysis (Fig. S1): interferon gamma signalling, antigen presentation: folding, assembly and peptide loading of Major Histocompatibility Complex (MHC) class I, signalling by PDGF, nervous system development, axon guidance and somitogenesis [25, 26, 52, 55].

Cholesterol biosynthesis and nucleotide metabolism show concordant enrichment in DFT2

Among the 178 enriched gene sets, a total of 14 pathways falls under the "metabolism" Reactome hierarchy (Fig. 2A). Two pathways showed concordant enrichment in DFT2 cell lines and biopsies: cholesterol biosynthesis ($s_{biopsies}$ = 0.16 and $s_{cell\ lines}$ = 0.47; Fig. 2B) and metabolism of nucleotides ($s_{biopsies}$ = 0.07 and $s_{cell\ lines}$ = 0.23; Fig. 2C). The cholesterol metabolism genes *SQLE*, *LSS* and *MVD* were upregulated in DFT2, in both datasets (Fig. 2B). Similarly, the *AK5*, *GMPR*, *TYMP*, *ENTPD4*, *NUDT18*, *IMPDH1*, *TXNRD1* and *GSR* genes, linked to the metabolism of nucleotides, were upregulated in DFT2 biopsies and cell lines. Within the same gene set, DFT2 cell lines and biopsies saw downregulated *AK9*.

Two metabolism related gene sets were concordantly enriched in DFT1 cell lines and biopsies: sulfur amino acid metabolism ($s_{biopsies}$ = -0.31 and $s_{cell\ lines}$ = -0.38) and degradation of cysteine and homocysteine (a subset of the sulfur amino acid metabolism gene set; $s_{biopsies}$ = -0.46 and $s_{cell\ lines}$ = -0.60; Fig. 2A). Sulfur amino acid genes, including *MTR*, *MPST*, *CTH*, and *ADO*, were downregulated in DFT2 cell lines and biopsies (Fig. 2D).

DFT2 cells have higher glycolysis rates than DFT1 cells

Cholesterol biosynthesis was observed to be enriched in DFT2 cells and biopsies. It is known from previous research that cholesterol homeostasis is important for DFT1 cell proliferation [16] and can stimulate a metabolic shift towards glycolysis. This prompted us to initially quantify the relative contribution of glycolysis in DFT1 and DFT2 cell proliferation. Lactate, a by-product of glycolysis, was firstly measured in the cell culture medium (Fig. 3A). DFT2 cells tended to produce more lactate than DFT1 cells, with two DFT2 cell lines (SN, TD549) showing significantly increased extracellular lactate production over time. SN produces 30.51 nmol of lactate, 95% CI [26.76, 34.59], whilst the highest lactate production by a DFT1 cell line was 2.7 nmol ($p < 0.01$; 95% CI [0.13, 11.85]). Remarkably, the DFT2 TD549 cell lines produced over a hundred times more lactate (174.83 nmol, 95% CI [139.51, 215.68]) compared to other cell lines. This higher lactate production by DFT2 cells indicates higher rates of glycolysis compared to the DFT1 cell lines.

We then tested how this difference in glycolysis rates would impact energy production in the form of ATP (Fig. 3B). To compare the amount of energy produced by glycolysis versus OXPHOS, we reported total, oxidative and glycolytic ATP production. Two DFT2 cell lines overall produced 1.5 times more ATP than DFT1 cells when cultured in media with glucose only; RV produced 1.59 nmol of ATP (95% CI [1.27, 2.01]) and SN cells 1.6 nmol (95% CI [1.28, 2]), compared to the highest ATP production in DFT1 cells of only 0.98 nmol by 1426 ($p < 0.001$, 95% CI [0.73, 1.31]) (Fig. 3B).

Exposure of cells to 2-deoxyglucose (2DG, which is converted to 2-deoxyglucose-6-phosphate (2DG6P) and accumulates in the cell, ultimately inhibiting glycolysis [56]), significantly decreased oxidative ATP production between 0.33 to 0.65 nmol in all cell lines (except one DFT1 cell line, 1426) compared to media with glucose only ($p < 0.001$) (Fig. 3B). Inhibiting OXPHOS with oligomycin (glycolytic ATP production only) significantly decreased ATP production in two DFT1 cell lines (1426 by 0.43 nmol and C5065 by 0.36 nmol; $p < 0.001$), and one DFT2 cell line (TD549 by 0.32) compared to glucose only treatment (Fig. 3B),

In summary, DFT2 cell lines have higher rates of glycolysis and ATP production that DFT1 cell lines and rely less on OXPHOS for ATP generation than DFT1 cells. Furthermore, DFT1 cells are more sensitive to inhibition of either glycolysis or OXPHOS for ATP generation than DFT2 cells. Interestingly, the DFT2 TD549 cell line appears to rely more on oxidative ATP generation than the other DFT2 cell lines (i.e. more sensitive to oligomycin). In conjunction with its high rate of lactate generation and lower ATP levels in media with glucose only, this finding suggests that ATP generation is less efficient overall in TD549 cells.

To further investigate the importance of metabolic selection in DFT1 and DFT2, we measured cell viability in the presence of various substrates (Fig 3C). Both DFT1 and DFT2 showed a significant decrease in cell viability by at least 71.6 % ($p < 0.001$) when glycolysis was inhibited with 2DG, compared to growth in glucose alone (Fig 3C). To test whether cells could switch to OXPHOS to obtain the ATP necessary for their survival, glucose was replaced by galactose. Galactose can enter glycolysis after being converted to glucose-6-phosphate through the Leloir pathway. However, this is less efficient and results in no net ATP gain [57]. Galactose significantly decreased viability in one DFT1 cell line (C5065 by 34.09 %; $p < 0.001$) and in two DFT2 cell lines (RV by 47.28 % and SN by 51.09 %; $p < 0.001$).

Lastly, pyruvate was added to the 2DG and galactose treatments to assess whether this could restore cell viability by driving OXPHOS [58]. Pyruvate did not rescue viability in any cell line when added in conjunction with 2DG. In contrast, when added in conjunction with galactose, pyruvate significantly increased the survival of two DFT1 cell lines (4906 by 26.33 % and C5065 by 36.22 %; $p < 0.001$) compared to galactose only treatment (Fig 3C).

In summary, both DFT1 and DFT2 cell lines rely on glycolysis for survival. However, DFT1 appears more metabolically flexible and can switch to oxidative metabolism (OXPHOS)

when required, whereas DFT2 cannot. Interestingly, the TD549 DFT2 cell line showed significantly higher survival compared to the other two DFT2 cell lines in most treatments (by at least 30.47 % in galactose, $p < 0.001$; 19.58 % in galactose and pyruvate, $p < 0.01$; and 22.8 % in 2DG, $p < 0.001$), suggesting these cells are more metabolically flexible than the other DFT2 cell lines examined.

Linking the functional and transcriptomic data, we identified genes that could be responsible for DFT2's higher glycolytic rates. Although the glycolysis gene set was not enriched in DFT2 ($p > 0.05$), three glycolysis genes were upregulated in DFT2: *ENO3*, *PFKM* and *ADPGK* (Fig. 3D). One gene, *HKDC1*, was downregulated in DFT2 in both datasets, whereas *HK3* was upregulation in DFT2 biopsies but was downregulated in DFT2 cell lines. This suggests that *ENO3*, *PFKM* and *ADPGK* are primarily driving the increase in glycolytic rates observed in DFT2 compared to DFT1.

DFT2 cells produce more ROS than DFT1 cells

We next investigated the effect of increased glycolysis and ATP production on ROS generation (Fig. 4A), as higher levels of glycolysis have been associated with elevated ROS production and oxidative stress [59]. Overall, ROS production was significantly higher in DFT2 cell lines, with RV producing the highest amount of ROS (70624 RFU, 95% CI [23282, 31874], $p < 0.001$), followed by SN (39949 RFU, 95% CI [32283, 47615] compared to DFT1 lines 1426 (22679, 95% CI [18272, 27087], $p < 0.01$) and C5065 (12439 RFU, 95% CI [9479, 15400], $p < 0.01$). To identify the type of ROS being produced, we quantified mitochondrial superoxide ROS production (Fig. 4B), however, no significant difference in the production of mitochondrial ROS was observed between any cell line ($p > 0.05$). DFT2 thus produces more ROS than DFT1, with this increase being cytoplasmic (and not mitochondrial) in origin.

In line with the observed elevated ROS production, both DFT2 cell lines and biopsies show enrichment of ROS detoxification genes (Fig. 4C; Fig. S1). *SOD3*, *CYBA*, *GPX7*, *TXNRD1* and *GSR* are overexpressed in both DFT2 datasets. Interestingly, *NCF4* is upregulated in DFT2 biopsies but downregulated in DFT2 cell lines. This suggests that increased cytoplasmic ROS production by DFT2 is somewhat mitigated by the upregulation of ROS detoxification genes to avoid ROS-induced cell death.

DFT2 relies more on lipid metabolism than DFT1

Lipid metabolism is essential in rapidly dividing cancer cells [60], which led us to test the role of fatty acid metabolism in DFT1 and DFT2 proliferation. We used etomoxir, an irreversible carnitine palmitoyl-transferase 1A inhibitor (CPT1A), to inhibit fatty acid oxidation [61] (Fig. 5A). Etomoxir acts by causing lipid accumulation and decreased ATP and NADPH production, ultimately stopping cell proliferation [62]. Etomoxir significantly decreased the viability of two DFT2 cell lines (RV by 35.34 % and SN by 38.17 %; $p < 0.001$), but not in TD549 (by 1.58 %; $p > 0.05$) compared to glucose only controls. Conversely, DFT1 cell lines

had no change in survival when cultured in etomoxir compared to glucose only controls (Fig. 4A).

We also investigated the importance of the pentose phosphate pathway (PPP) for providing NADPH (as well as nucleotides) for DFT cell viability [63] (Fig. 5A). For these experiments we used oxythiamine to prevent thiamine from transitioning to its active form, ultimately inhibiting transketolase, an essential enzyme in the PPP [64]. Oxythiamine had no effect on DFT1 survival, but showed a trend of reduced viability in DFT2 cells, with viability significantly decreased in the RV DFT2 cell line (by 32.66 %; $p < 0.001$).

To investigate if DFTs also rely on fatty acid anabolism, cells were further treated with pioglitazone, an ACSL4 inhibitor blocking fatty acid synthesis [61] (Fig. 5B). When treated with pioglitazone, all DFT cell lines showed decreased viability compared to untreated glucose only cells ($p < 0.001$). Pioglitazone had a greater antiproliferative effect on DFT2 cell lines (by 89.29 %), compared to DFT1 (by 35.33 %; $p < 0.001$). We hence conclude that DFT2 cells rely more on both fatty acid oxidation and fatty acid synthesis than DFT1 cells.

We also examined if DFT1 and DFT2 cells rely on oxidative ATP generation for their viability (Fig. 5B). DFT cells were treated with the ATP synthase inhibitor oligomycin, which significantly decreased cell viability for all six cell lines compared to untreated (glucose only) controls (Fig 5B; by 42.5% on average, $p < 0.001$). This demonstrates that oxidative phosphorylation, and the ATP generated by this pathway, remains important for DFT cell survival.

Linking the fatty acid metabolism results with the transcriptomics data, we found that the following fatty acid metabolism genes were concordantly upregulated in DFT2 cell lines and biopsies compared to DFT1: *THRSP*, *PTGIS*, *PTGS2*, *TBXAS1*, *FADS2*, *SCD5*, *MAPKAPK2* and *ACSL3* (Fig. 5C). Conversely, *ACSL1*, *PRKAG2*, *PRXL2B*, *ELOVL4*, *FAAH*, *ELOVL2* and *ELOVL3* were downregulated in DFT2 compared to DFT1. It is important to note however that the total fatty acid metabolism gene set is not significantly enriched in DFT2 ($p > 0.05$).

Based on our previous observation that cholesterol biosynthesis genes are enriched in DFT2, we measured cholesterol content in DFT1 and DFT2 cells (Fig. 5D). DFT2 cells contained three to four times more cholesterol than DFT1 cells ($p < 0.05$), consistent with DFT2 upregulating genes linked to cholesterol biosynthesis (Fig. 2A & B).

Both DFT1 and DFT2 rely on glutamate production and oxidative metabolism for survival

DFT1 and DFT2's reliance on glutamine, an essential substrate for cancer cell metabolism [65], was tested by incubating cells in glutamine depleted medium (Fig. 5E). This significantly decreased the viability of only one DFT1 cell line (4906 by 20.5 %; $p < 0.01$) and significantly increased the viability of another DFT1 cell line (1426 by 19.03 %; $p < 0.001$) compared to control medium with glucose (and glutamine). DFT2 cell lines were not

impacted by the absence of glutamine in their culture medium. The DFT1 and DFT2 cells were then grown with BPTES, an inhibitor preventing glutaminase-1 from converting glutamine to glutamate, and this treatment significantly decreased the viability of all DFT1 and DFT2 cell lines compared to control glucose (with glutamine) treatment (by 72.99 % on average; $p < 0.001$). This result suggests that DFT1 and DFT2 can generate endogenous glutamine, but both rely on the conversion of this glutamine to glutamate for survival.

DISCUSSION

This work demonstrates that, *in vitro*, similar metabolic pathways drive DFT1 and DFT2 proliferation, with glycolysis, OXPHOS, glutamine metabolism and fatty acid synthesis being essential for their survival. However, the two transmissible tumours differ slightly, but significantly, in their metabolic usage. DFT2 has a higher rate of glycolysis relative to DFT1, which is accompanied by higher lactate generation and ATP production. This is consistent with DFT2's hypothesised cell-type of origin (i.e., a repair Schwann cell, whilst DFT1 originated from a myelinating Schwann cell [26, 66]). During nerve injury, repair Schwann cells increase glycolysis in comparison to myelinating Schwann cells to support axons [27]. Our transcriptomic analysis revealed that DFT2 could achieve this by upregulating *ADPGK*, *PFKM*, and *ENO3*. ADPGK catalyses phosphorylation of glucose to glucose-6-phosphate using ADP as a phosphate donor. This initial step of glycolysis is typically catalysed by ATP-dependent hexokinases. Therefore, it is believed that ADPGK could assist in conserving ATP during hypoxia, thereby reducing the ATP consumption necessary for glucose phosphorylation [67]. Next, PFKM catalyses the phosphorylation of D-fructose 6-phosphate to fructose-1,6-bisphosphate using ATP, which is the first committed step of glycolysis. Finally, ENO3 is responsible for the conversion of 2-phosphoglycerate to phosphoenolpyruvate in the glycolytic pathway. Because fructose-1,6-bisphosphate production has previously been identified as one of the key flux-controlling steps of glycolysis [68], we expect *ADPGK* and *PFKM* upregulation to play a major role in DFT2's higher rate of glycolysis in comparison to DFT1. Interestingly, we also observed upregulation of hexokinase 3 (*HK3*) in DFT2 biopsies, which further suggests this could be a mechanism underlying higher rates of glycolysis.

This is the first study directly comparing DFT1 and DFT2 metabolism using tumour cell lines and biopsies. At the time of this work, DFT2 transcriptomes were scarce with only a single study conducting full RNA sequencing of one DFT1 and DFT2 cell line and two DFT1 and DFT2 biopsies [26]. By conducting full transcriptome analyses of two additional DFT1 and DFT2 cell lines, this study provides valuable data for future *in vitro* work on DFTD. Overall, more genes were differentially expressed in the cell lines than in biopsies, likely due to differences in sequencing depth between the transcriptomes. In the future, re-sequencing both cell lines and biopsies on the same platform would offer a more robust approach, as this difference could have led to an underestimation of the number of differentially expressed genes in the biopsy data. Nevertheless, by integrating *in vitro* metabolic assays with the analysis of cell line and biopsy transcriptomes, we minimize the risk of identifying metabolic differences associated with adaptation to cell culture conditions. Consequently, we can confidently identify metabolic pathways crucial for these transmissible tumours.

Previous research [16] had demonstrated the importance of glycolysis for DFT1 proliferation. We confirm their findings by showing the reliance of both DFT1 and DFT2 on glycolysis for survival. Ikonomopoulou and colleagues [16] further linked cholesterol homeostasis to this metabolic shift towards glycolysis in DFT1. We observe a similar pattern in DFT2. Cholesterol biosynthesis genes are enriched in DFT2 cell lines and biopsies, which is consistent with DFT2 containing threefold more cholesterol than DFT1 and its higher rate of glycolysis. Indeed, the acidic environment caused by elevated glycolysis and ATP hydrolysis has been shown to increase cholesterol biosynthesis in human malignancies, allowing cancer cells to sustain proliferation, migrate and invade tissues [69].

Another finding of our study is that DFT2 produces more cytoplasmic ROS than DFT1. Current research [59] shows that increased glucose conversion to pyruvate can elevate cellular ROS levels. We thus hypothesise that higher glycolysis rates driven by *ADPGK* and *PFKM* upregulation could be responsible for both increased ROS production and upregulation of ROS detoxification genes in DFT2. Furthermore, we observed concordant enrichment of genes belonging to the degradation of cysteine and homocysteine pathway in DFT1 cell lines and biopsies. Degradation of these amino acids through the transulphuration pathway leads to the generation of glutathione (GSH) and taurine, both sustaining redox chemistry [70]. This could explain lower ROS production by DFT1 compared to DFT2 cell lines, although this needs to be verified by quantifying GSH production.

Within the DFT2 cell lines tested in this study we mostly observed comparable effects to the inhibitors used, although TD549's response tended to differ from the other two cell lines (RV and SN). As such, TD549 produced less ATP and ROS, more lactate, and had an overall better survival in the presence of inhibitors than the other DFT2 cell lines. We hypothesise that rearrangements on chromosome 2 distinguishing TD549 from RV and SN could explain such differences [71]. TD549 notably lacks one copy of the gene *FSHR* [71], the product of which is responsible for downstream PI3K-AKT signalling [72], a pathway implicated in altered carbohydrate metabolism in DFT1 [16]. In Figure 1A the multidimensional scaling (MDS) analysis reveals that the biological replicates of DFT1 tumours cluster together in a distinct pattern separate from the DFT2 tumours. Interestingly, the DFT2 biological replicates also cluster separately from each other. This difference in DFT2 tumour clustering could also be influenced by factors associated with the original tumour biopsy, including the stage of the cancer, its specific location and possible tumour cell sub-linages.

Our findings are somewhat limited due to the use of *in vitro* conditions that do not accurately reflect the genetic and vascular heterogeneity of an *in vivo* tumour [73]. In addition, one might not capture the full extent of the diversity of tumours circulating currently in Tasmania, a problem which could be addressed by deriving more recent cell lines from primary tumours.

Increased glycolysis rates in cancer cells play an important role in immune evasion by limiting the availability of glucose to tumour-infiltrating lymphocytes [8]. DFT1 is thought to evade the immune system by downregulating MHC molecules, which are still expressed by DFT2 [55, 74]. Furthermore, certain DFT2 lineages carry a Y chromosome (as DFT2

originated from a male devil) and, likely because of its immunogenicity, appear to be less successful at infecting female devils [22, 75]. Therefore, we hypothesise that increased lactate production in DFT2, because of increased glycolysis rates, might play a role in evading the devil's immune system. Indeed, previous research reported that few tumour-infiltrating lymphocytes were observed within DFT2 biopsies [55]. That would explain the differential gene expression patterns between the two DFT2 biopsy samples (Fig.1D), as two B cell and plasma cell markers (MS4A1 and MZB1) were highly expressed in DFT2_2 biopsy, indicating immune infiltration. An active immune response in a tumour would consume a lot of energy, and thus potentially impact the expression of metabolism related genes for that sample. As our tumour purity calculations indicated the sample mostly consisting of tumour cells and as we focused on genes that were differentially expressed/pathways enriched in both the biopsies and in the cell lines, we believe the general conclusions remain the same.

ROS are a source of oxidative DNA damage and result in higher DNA mutation rates. We observed higher ROS generation in DFT2 cell lines compared to DFT1, and this concurs with the higher mutation rates observed in DFT2 tumours compared to DFT1 tumours [22]. High mutation rates in clonally reproducing organisms should lead to the accumulation of deleterious mutations, and eventually genomic decay [76, 77]. However, the three types of transmissible cancers known so far all share mutation rates exceeding those of human cancers, and it is proposed that such a high mutation load could carry indirect positive fitness outcomes [78].

DFT2's higher rate of glycolysis explains its previously reported faster *in vitro* growth and could explain how it is able to outcompete DFT1 in co-culture assays [30]. Higher rates of cell division require increased deoxyribonucleotide triphosphate (dNTP) synthesis, which are not only rate-limiting for DNA replication and repair, but also for transcription, ribosome biogenesis and post-translational protein glycosylation [79]. Indeed, we found that reducing nucleotide supply by inhibiting the pentose phosphate pathway decreased DFT2 cell viability (Fig 5A). This corresponds with the enriched nucleotide metabolism and catabolism in DFT2 cells that drive faster cell division [30].

Considering these observations, we hypothesise that DFT2 could be a more aggressive cancer than DFT1. Meta-analyses of human cancer patients have associated elevated aerobic glycolysis with poorer prognosis [80, 81]. For instance, elevated expression of glycolysis-related genes was associated with aggressive phenotypes such as poor tumour differentiation, deeper invasion, lymph node metastasis and vascular invasion in high-grade brain tumours [81]. A second meta-analysis [80] demonstrated ultimately worse overall survival for hepatocellular carcinoma patients with elevated expression of glycolysis markers. Based on these human studies, it can be predicted that DFT2 tumours could have a higher potential to invade tissues and metastasise.

The fact that DFT1 and DFT2 appear to share some common pathways for their growth and survival is promising for the development of future treatments against DFTD. Atorvastatin, which has proven to be effective in reducing DFT1 tumour growth [16], is likely to also

inhibit DFT2 tumour growth, underscoring its potential to assist in ongoing management plans for the conservation of Tasmanian devils. However, DFT2's increased glycolytic rate and potential metabolic plasticity could represent an important threat to Tasmanian devils if these metabolic features translate *in vivo*. If so, DFT2 is likely to have a faster growth rate, enhanced immune evasion and higher adaptive potential than DFT1. It is important to note that DFT2 has been progressing on a different epidemiological landscape than DFT1. DFT2 arose in a smaller, more disperse population that had already been exposed to DFT1 for almost 30 years[-]. However, DFT2's evolutionary trajectory remains unknown. Our results, taken together with DFT2's expansion outside of the peninsula where it originated, highlight the necessity to further research the differences and similarities of these unique transmissible cancers and their endangered host.

Finally, to survive across hosts and environments, we show that Tasmanian devil facial tumour cells undergo extreme metabolic flexibility, which mirrors what human cancers do during metastasis and therapy resistance. Like human tumours, transmissible cancers rely heavily on glycolysis—even when oxygen is available, and such Warburg effect appears to be amplified in these clonal cells. They exhibit metabolic plasticity as they adapt their energy sources depending on the host's tissue environment, showcasing how tumours can switch between glycolysis, oxidative phosphorylation, and lipid metabolism. Transmissible cancers offer real-world examples on how cancer cells survive in hostile or changing environments. The pathways identified in our study reveal the metabolic vulnerabilities of these, and potentially human cancers, offering druggable targets and treatment options. As DFTD cells use similar metabolic strategies as human cancers, they can serve as natural models to test metabolic inhibitors (e.g., drugs targeting glycolysis, glutamine metabolism, or lipid synthesis) and may be used to help identify biomarkers for aggressive or treatment-resistant human cancers. While transmissible cancers are rare, they can show how cancer cells can thrive, evolve, and adapt metabolically, and such provide a window into the metabolic character of cancer.

MATERIALS AND METHODS

EXPERIMENTAL MODEL

Cell Lines and Cell Culture

Devil Facial Tumour 1 (DFT1) cell lines 4906, 1426 and C5065 and DFT2 cell lines RV, SN and TD549 were grown *in vitro* as previously described [21, 30, 31]. DFT cell lines were derived from different animals and act as biological replicates. Cells were cultured in RPMI-1640 media (Gibco, 21870092; 2 g/L of glucose), supplemented with 1 % GlutaMAX (Gibco, 35050061), 10 % FBS (Gibco, 10099141) and 1 % 10,000 U/mL penicillin/streptomycin (Gibco, 15070063) at 35 °C and 5 % CO_2. Upon reaching 80-90 % confluency, cells were washed with DPBS (Gibco, 14190250) detached using TrypLE Express (Gibco, 12605010), centrifuged at 500 x g for 5 minutes and passaged 1:3. Cells used in the present work were maintained below passage 30. All cell lines were obtained from Dr Hannah V. Siddle. DFT1 cell lines were tested for mycoplasma as described in [29]. DFT2 cells were tested for mycoplasma using the MycoAlert mycoplasma testing kit (Lonza, LT07-418) when they entered the laboratory and were passaged in a mycoplasma-free tissue culture facility after testing [30]. Additional information on the cell lines used in the present study can be found in Table 1.

METHOD DETAILS

Sample Processing and RNA Sequencing

DFT cell lines were grown in 6-well plates until 80-90 % confluent before harvesting. RNA was extracted from all samples using the Zymo Direct-zol™ RNA kit (Zymo Research, R2051) as per manufacturer instructions. Quantification and qualification of extracted RNA was performed on a Qubit RNA High Sensitivity (Invitrogen) and on a Tapestation 4200-RNA Screentape (Agilent). All samples had RNA integrity scores (RIN) scores greater than 9.5.

Library Preparation and Sequencing

Library preparation was performed using the NEBNext® Ultra™ II Directional RNA Library Prep Kit for Illumina (New England Biolabs, E7760) with 400 ng of each sample, 5X Adapter dilution and a 10 cycle PCR. Technical triplicates from all samples were sequenced at the Charles Rivers Laboratories on a NovaSeq6000 (Illumina) using 300 cycles and 150 paired end reads.

Previously published data

RNA sequences from two DFT1 and two DFT2 primary tumours published in Patchett et al. [26] were re-analysed for comparison will cell line data. These tumour data consist of two biological replicates per DFT, sequenced in duplicate (i.e., technical replicates) using 100

base-pair single end read mRNA sequencing on the Hiseq-2500 platform (Illumina). FASTQ files were downloaded from the European Nucleotide Archive (project PRJEB28680).

Metabolic assays

Cell viability after metabolic inhibition was measured by MTT (3-(4, 5-dimethylthiazolyl-2)-2, 5-diphenyltetrazolium bromide) assay (Cell Proliferation Kit I, Roche, 11465007001) following manufacturer's instructions. 10,000 cells/well were seeded in 96-well and incubated for 24 h. Cells were then treated with fresh culture medium (glucose controls) or culture medium with metabolic inhibitor (treatments; see Table 2). Concentration of inhibitors was determined based on common concentrations used in the literature [32–37]. Cells were incubated for an additional 72 h before MTT reduction was measured at 550 nm in a FLUOstar Omega plate-reader (BMG LABTECH) and Omega software (version 3.00 R2). Controls were used to define 100 % viability with three independent experiments performed, each comprised of 6 technical replicates per cell line.

Measurement of ATP production

Cells were treated with fresh culture medium (control), culture medium with 1 mM 2DG (Sigma, D8375; to measure oxidative ATP production) or 5 μM oligomycin (Sigma, 75351; to measure glycolytic ATP production) as previously described [38] and incubated for 3 h. ATP was quantified using the ATPlite 1step kit (PerkinElmer, 6016731) according to manufacturer's instructions. Luminescence was measured in a FLUOstar Omega plate-reader (BMG Labtech). Three independent experiments were performed, each comprised of 6 replicates per cell line.

Measurement of ROS production

Overall ROS production was measured using H_2DCFDA (Sigma, D6883). Cells were incubated with 10 μM H_2DCFDA for 30 min in the dark at 35°C, washed with DPBS, then incubated for 20 min in 100 μL of DPBS. Fluorescence at 480 nm excitation and 520 nm emission was measured using a FLUOstar Omega plate-reader for 1 h. Three independent experiments were performed, each comprised of 6 replicates per cell line.

Mitochondrial ROS production was quantified using MitoSOX™ Green (Thermo Fisher Scientific, M36006). Cell were seeded on black clear bottom 96-well plates (Interpath, 655090) and left to adhere for 48 h. Cells were then incubated with 1 μM MitoSOX™ Green in DPBS and incubated at 35°C and 5% CO_2 for 30 min. Cells were washed and plates centrifuged at 400 x *g* for five min, followed by incubation for one h in the dark. Fluorescence intensity was then measured at 485 nm excitation/520 nm emission with a FLUOstar Omega plate-reader. Three independent experiments were performed with six replicates per cell line.

Measurement of extracellular lactate

Cells were plated and incubated as described above. Cell culture supernatants were harvested after 2, 6 and 8 days, deproteinised using 10 kDa MWCO spin filters (Merck, UFC5010), and stored at -80 °C until further analysis. After each collection, cell number per well was measured by MTT. Cell culture supernatants were thawed, and lactate was measured using a Lactate Assay Kit (Sigma, MAK064) according to the manufacturer's protocol. Absorbance was measured at 570 nm on a FLUOstar Omega plate-reader. Wells containing only media were used to blank the readings. Two independent experiments were performed, each comprised of duplicates for each cell line. Lactate content was standardised by cell number and calculated for 10^6 cells.

Measurement of cholesterol content

One million cells were pelleted and stored at -80 °C until further processing. Samples were thawed and were resuspended in 200 μL of a 7:11:0.1 chloroform:isopropanol:IGEPAL mix (Merck, 1.02445; Chem Supply, AH323-4; Merck, CA-630) to extract lipids. Samples were centrifuged for 10 min at 13,000 x g to remove insoluble material. The organic phase was transferred to a new tube and left to air dry at 50 °C for 1 h. Then samples were dehydrated under a vacuum for 30 min at 50 °C using a SpeedVac (Savant). Dried lipids were resuspended in 200 μL of Cholesterol Assay Buffer from the Cholesterol Quantitation Kit (Sigma, MAK043). Manufacturer's directions were followed to measure cholesterol content. Absorbance was recorded at 570 nm on a FLUOstar Omega plate-reader. Three samples per cell line, each from independent cell subcultures, were used for this experiment.
Table 3 contains information on all key resources used in the study.

QUANTIFICATION AND STATISTICAL ANALYSIS

Sequence analysis

Sequence reads were filtered (3' end quality trimming with a quality threshold of 10) and trimmed using skewer [39] (v0.2.2) and pseudo-aligned to the Tasmanian devil reference genome (mSarHar 1.11) using kallisto [40] (v0.50.0), both using Bash [41] scripts. Technical replicates were combined and genes with a mean count of less than 10 across all samples were removed to exclude genes with extremely low expression. Human homologs of Tasmanian devil genes were obtained from Ensembl (release 109) using BioMart [42]. Differential gene expression analysis between DFT1 and DFT2 cell lines, and between DFT1 and DFT2 tumour biopsies was performed using DESeq2 [43] (v1.42.0). Differential expression p-values underwent false discovery rate (FDR) adjustment to account for multiple testing [44]. An adjusted p-value (FDR) < 0.05 was considered significant. To identify groups of genes (pathways) that are statistically over-expressed, a multi-contrast pathway enrichment analysis was performed using mitch [45] (v1.14.0) and Reactome [46] gene sets (V85) combined with two custom gene sets (data not shown). This allowed to directly compare differential gene expression between DFT1 and DFT2 cell lines to DFT1 and DFT2 biopsies. We also interrogated significant differentially expressed genes (DEGs) belonging to Reactome

pathways investigated in our metabolic assays. Differential gene expression and pathway enrichment analyses were performed in R [47] (v4.3.3). For pathway enrichment analysis, an adjusted p-value (FDR) < 0.05 was considered significant.

Tumour purity calculation

To ensure tumour biopsies were not contaminated by host tissue, tumour purity was calculated and compared to that of the cell lines (which are clonal, hence not contaminated by host tissue). Tumour biopsy and cell line sequences were trimmed using skewer [39] then aligned to the mSarHar1.11 genome using the STAR aligner [48]. Files were converted from .sam to .bam, sorted by genomic location and indexed using SAMtools [49]. Mean coverage was then calculated over arbitrary 1kb non overlapping windows over the entire genome and over two large deletions proper to DFT1 and DFT2, using the BEDtools [50] coverage function. The DFT1 specific deletion is found at 3:192,161,000-216,866,000 (as per Stammnitz et al.[51]) and the DFT2 specific deletion at 5:141461000-175266000 (chosen from Stammnitz et al. [52]). Tumour purity was then calculated as (coverage deletion / overall coverage) x 100. Tumour purity calculations were performed using Bash [41] scripts and are available in Table S1.

Mixed effects models

All statistical analyses were performed in R [47] (version 4.3.0) using Gaussian mixed effects linear models. Response variables were either cell viability or metabolite production. To choose appropriate explanatory variables (cell lines, DFT), models were built following the Zuur protocol [53] (Table S3). Briefly, models with or without experimental replicate as a random intercept were built to account for possible batch effects between experiments. The most parsimonious fixed effects model was then selected. Models with the lowest Akaike's Information Criterion (AIC) and highest AIC weights were selected. Model assumptions (i.e., homogeneity of variances and normality of residuals) were verified using diagnostic plots. Model selection showed all experiments required cell lines to be considered separately and could not be pooled by DFT due to variability in the results among cell lines of the same DFT. Model means and 95 % confidence intervals are reported in Table S4. Contrasts were performed using Tukey's post hoc test, with Bonferroni correction for multiple testing (Table S4).

AUTHOR CONTRIBUTIONS

Conceptualization: A.-L.G., F.P., A.G.S., M.M., M.Z., B.U. Data Curation: A.-L.G., F.P., C.V. Formal Analysis: A.-L.G., F.P., C.V., A.M.D. Funding acquisition: A.-L.G., M.M.,R.H., F.T., B.U. Investigation: A.-L.G., F.P., C.V. Methodology: A.-L.G., F.P., M.M., M.Z. Project administration: A.-L.G., U.B. Resources: A.-L.G., F.P., C.V., A.G.S., H.S., M.M., M.Z. Software: A.-L.G., F.P., C.V., M.Z. Supervision: A.-L.G., F.T., B.U. Validation: A.-L.G., F.P., C.V. Writing – Original draft: A.-L.G. Writing – Reviewing & Editing. A.-L.G., F.P., C.V., A.M.D., A.G.S., R.H., H.S., F.T., M.M., M.Z., B.U.

ACKNOWLEDGEMENTS

This work was supported by an ARC Linkage (LP170101105), ARC Decra (DE170101116), ARC DP (DP230100162), an ANR TRANSCAN (ANR--18--CE35--0009), the Save The Tasmanian Devil Eric Guiler Research Funds, Deakin University's LES Blue Sky and SEBE Industry partnership funds, a CNRS International Research Project, a Morris Animal Foundation grant (D19ZO--413) and the Hoffmann Family. This research was supported by use of the Nectar Research Cloud, a collaborative Australian research platform supported by the NCRIS-funded Australian Research Data Commons (ARDC). The authors gratefully acknowledge the contribution to this work of the Victorian Operational Infrastructure Support Program received by the Burnet Institute.
During the preparation of this work the authors used Apple Intelligence and ChatGPT 5.2 to improve the readability and language of some sentences in the manuscript. After using these tools, the authors reviewed and edited the content as needed and take full responsibility for the content of the published article.
The graphical abstract was made using BioRender.

DATA AVAILABILITY STATEMENT

All data and code are publicly available as of the date of publication. All original code has been deposited on GitHub and is available at https://github.com/Anne-LiseGerard as of the date of publication. RNA-seq data have been deposited at NCBI's Sequence Read Archive (SRA) and are available under PRJNA1122388. The raw count matrix generated from this data is available at https://github.com/Anne-LiseGerard. This paper also analyses existing RNA sequences, available under PRJEB28680 on the SRA. Metabolic assay data are available upon request.

REFERENCES

1. Barnum KJ, O'Connell MJ (2014) Cell cycle regulation by checkpoints. Methods Mol Biol 1170:29–40. https://doi.org/10.1007/978-1-4939-0888-2_2

2. Fan H-C, Chang F-W, Tsai J-D, et al (2021) Telomeres and Cancer. Life 11:1405. https://doi.org/10.3390/life11121405

3. Rao S, Gharib K, Han A (2019) Cancer Immunosurveillance by T Cells. In: International Review of Cell and Molecular Biology. Elsevier, pp 149–173

4. Hanahan D (2022) Hallmarks of Cancer: New Dimensions. Cancer Discovery 12:31–46. https://doi.org/10.1158/2159-8290.CD-21-1059

5. Hanahan D, Weinberg RA (2011) Hallmarks of Cancer: The Next Generation. Cell 144:646–674. https://doi.org/10.1016/j.cell.2011.02.013

6. Vander Heiden MG, DeBerardinis RJ (2017) Understanding the Intersections between Metabolism and Cancer Biology. Cell 168:657–669. https://doi.org/10.1016/j.cell.2016.12.039

7. Vazquez A, Kamphorst JJ, Markert EK, et al (2016) Cancer metabolism at a glance. Journal of Cell Science 129:3367–3373. https://doi.org/10.1242/jcs.181016

8. Liberti MV, Locasale JW (2016) The Warburg Effect: How Does it Benefit Cancer Cells? Trends in Biochemical Sciences 41:211–218. https://doi.org/10.1016/j.tibs.2015.12.001

9. Danhier P, Bański P, Payen VL, et al (2017) Cancer metabolism in space and time: Beyond the Warburg effect. Biochimica et Biophysica Acta (BBA) - Bioenergetics 1858:556–572. https://doi.org/10.1016/j.bbabio.2017.02.001

10. Yoo HC, Yu YC, Sung Y, Han JM (2020) Glutamine reliance in cell metabolism. Exp Mol Med 52:1496–1516. https://doi.org/10.1038/s12276-020-00504-8

11. Bian X, Liu R, Meng Y, et al (2021) Lipid metabolism and cancer. Journal of Experimental Medicine 218:e20201606. https://doi.org/10.1084/jem.20201606

12. Metzger MJ, Villalba A, Carballal MJ, et al (2016) Widespread transmission of independent cancer lineages within multiple bivalve species. Nature 534:705–709. https://doi.org/10.1038/nature18599

13. Murgia C, Pritchard JK, Kim SY, et al (2006) Clonal origin and evolution of a transmissible cancer. Cell 126:477–487

14. Pearse A-M, Swift K (2006) Transmission of devil facial-tumour disease: Allograft theory. Nature 439:549–549. https://doi.org/10.1038/439549a

15. Burioli EAV, Hammel M, Vignal E, et al (2023) Transcriptomics of mussel transmissible cancer MtrBTN2 suggests accumulation of multiple cancer traits and oncogenic pathways shared among bilaterians. Open Biol 13:230259. https://doi.org/10.1098/rsob.230259

16. Ikonomopoulou MP, Lopez-Mancheño Y, Novelle MG, et al (2021) LXR stimulates a metabolic switch and reveals cholesterol homeostasis as a statin target in Tasmanian devil facial tumor disease. Cell Reports 34:108851. https://doi.org/10.1016/j.celrep.2021.108851

17. McCallum H, Tompkins DM, Jones M, et al (2007) Distribution and Impacts of Tasmanian Devil Facial Tumor Disease. EcoHealth 4:318–325. https://doi.org/10.1007/s10393-007-0118-0

18. Lazenby BT, Tobler MW, Brown WE, et al (2018) Density trends and demographic signals uncover the long-term impact of transmissible cancer in Tasmanian devils. Journal of Applied Ecology 55:1368–1379. https://doi.org/10.1111/1365-2664.13088

19. Cunningham CX, Comte S, McCallum H, et al (2021) Quantifying 25 years of disease caused declines in Tasmanian devil populations: host density drives spatial pathogen spread. Ecology Letters ele.13703. https://doi.org/10.1111/ele.13703

20. Hamede R, McCallum H, Jones M (2013) Biting injuries and transmission of Tasmanian devil facial tumour disease. Journal of Animal Ecology 82:182–190. https://doi.org/10.1111/j.1365-2656.2012.02025.x

21. Pye RJ, Pemberton D, Tovar C, et al (2016) A second transmissible cancer in Tasmanian devils. Proceedings of the National Academy of Sciences 113:374–379. https://doi.org/10.1073/pnas.1519691113

22. Stammnitz MR, Gori K, Kwon YM, et al (2023) The evolution of two transmissible cancers in Tasmanian devils. Science 380:283–293. https://doi.org/10.1126/science.abq6453

23. Hawkins CE, Baars C, Hesterman H, et al (2006) Emerging disease and population decline of an island endemic, the Tasmanian devil Sarcophilus harrisii. Biological Conservation 131:307–324. https://doi.org/10.1016/j.biocon.2006.04.010

24. Loh R, Bergfeld J, Hayes D, et al (2006) The Pathology of Devil Facial Tumor Disease (DFTD) in Tasmanian Devils (*Sarcophilus harrisii*). Veterinary Pathology 43:890–895. https://doi.org/10.1354/vp.43-6-890

25. Owen RS, Ramarathinam SH, Bailey A, et al (2021) The differentiation state of the Schwann cell progenitor drives phenotypic variation between two contagious cancers. PLoS Pathog 17:e1010033. https://doi.org/10.1371/journal.ppat.1010033

26. Patchett AL, Coorens THH, Darby J, et al (2019) Two of a kind: transmissible Schwann cell cancers in the endangered Tasmanian devil (Sarcophilus harrisii). Cellular and Molecular Life Sciences. https://doi.org/10.1007/s00018-019-03259-2

27. Trimarco A, Taveggia C (2020) Schwann cell energy to die for. Nat Neurosci 23:1179–1181. https://doi.org/10.1038/s41593-020-00707-2

28. Brabletz T (2012) To differentiate or not — routes towards metastasis. Nat Rev Cancer 12:425–436. https://doi.org/10.1038/nrc3265

29. Kwon YM, Stammnitz MR, Wang J, et al (2018) Tasman-PCR: a genetic diagnostic assay for Tasmanian devil facial tumour diseases. Royal Society Open Science 5:180870. https://doi.org/10.1098/rsos.180870

30. Gérard A, Owen RS, Dujon AM, et al (2024) In vitro competition between two transmissible cancers and potential implications for their host, the Tasmanian devil. Evolutionary Applications 17:e13670. https://doi.org/10.1111/eva.13670

31. Pyecroft SB, Pearse A-M, Loh R, et al (2007) Towards a Case Definition for Devil Facial Tumour Disease: What Is It? EcoHealth 4:346–351. https://doi.org/10.1007/s10393-007-0126-0

32. Amaral A, Castillo J, Estanyol JM, et al (2013) Human Sperm Tail Proteome Suggests New Endogenous Metabolic Pathways. Molecular & Cellular Proteomics 12:330–342. https://doi.org/10.1074/mcp.M112.020552

33. Gu L, Yi Z, Zhang Y, et al (2017) Low dose of 2-deoxy-D-glucose kills acute lymphoblastic leukemia cells and reverses glucocorticoid resistance via N-linked glycosylation inhibition under normoxia. Oncotarget 8:30978–30991. https://doi.org/10.18632/oncotarget.16046

34. Tran TQ, Ishak Gabra MB, Lowman XH, et al (2017) Glutamine deficiency induces DNA alkylation damage and sensitizes cancer cells to alkylating agents through inhibition of ALKBH enzymes. PLoS Biol 15:e2002810. https://doi.org/10.1371/journal.pbio.2002810

35. Yan M, Smeets R, Gosau M, et al (2022) Tolerance of Human Fibroblasts to Benfo-Oxythiamine In Vitro. IJERPH 19:4112. https://doi.org/10.3390/ijerph19074112

36. Yuan L, Sheng X, Clark LH, et al (2016) Glutaminase inhibitor compound 968 inhibits cell proliferation and sensitizes paclitaxel in ovarian cancer. Am J Transl Res 8:4265–4277

37. Zhan H, Girnun G, Dong K, et al (2014) Targeting Glutamine Metabolism in Myeloproliferative Neoplasms. Blood 124:1869–1869. https://doi.org/10.1182/blood.V124.21.1869.1869

38. McKenzie M, Liolitsa D, Akinshina N, et al (2007) Mitochondrial ND5 Gene Variation Associated with Encephalomyopathy and Mitochondrial ATP Consumption. Journal of Biological Chemistry 282:36845–36852. https://doi.org/10.1074/jbc.M704158200

39. Jiang H, Lei R, Ding S-W, Zhu S (2014) Skewer: a fast and accurate adapter trimmer for next-generation sequencing paired-end reads. BMC Bioinformatics 15:182. https://doi.org/10.1186/1471-2105-15-182

40. Bray NL, Pimentel H, Melsted P, Pachter L (2016) Near-optimal probabilistic RNA-seq quantification. Nat Biotechnol 34:525–527. https://doi.org/10.1038/nbt.3519

41. GNU (2024) Bash

42. Smedley D, Haider S, Ballester B, et al (2009) BioMart – biological queries made easy. BMC Genomics 10:22. https://doi.org/10.1186/1471-2164-10-22

43. Love MI, Huber W, Anders S (2014) Moderated estimation of fold change and dispersion for RNA-seq data with DESeq2. Genome Biology 15:. https://doi.org/10.1186/s13059-014-0550-8

44. Benjamini Y, Hochberg Y (1995) Controlling the False Discovery Rate: A Practical and Powerful Approach to Multiple Testing. Journal of the Royal Statistical Society Series B (Methodological) 57:289–300

45. Kaspi A, Ziemann M (2020) mitch: multi-contrast pathway enrichment for multi-omics and single-cell profiling data. BMC Genomics 21:447. https://doi.org/10.1186/s12864-020-06856-9

46. Gillespie M, Jassal B, Stephan R, et al (2022) The reactome pathway knowledgebase 2022. Nucleic Acids Research 50:D687–D692. https://doi.org/10.1093/nar/gkab1028

47. R Core Team (2024) R: A language and environment for statistical computing

48. Dobin A, Davis CA, Schlesinger F, et al (2013) STAR: ultrafast universal RNA-seq aligner. Bioinformatics 29:15–21. https://doi.org/10.1093/bioinformatics/bts635

49. Li H, Handsaker B, Wysoker A, et al (2009) The Sequence Alignment/Map format and SAMtools. Bioinformatics 25:2078–2079. https://doi.org/10.1093/bioinformatics/btp352

50. Quinlan AR, Hall IM (2010) BEDTools: a flexible suite of utilities for comparing genomic features. Bioinformatics 26:841–842. https://doi.org/10.1093/bioinformatics/btq033

51. Stammnitz MR, Gori K, Murchison EP (2024) No evidence that a transmissible cancer has shifted from emergence to endemism in Tasmanian devils. R Soc Open Sci 11:231875. https://doi.org/10.1098/rsos.231875

52. Stammnitz MR, Coorens THH, Gori KC, et al (2018) The Origins and Vulnerabilities of Two Transmissible Cancers in Tasmanian Devils. Cancer Cell 33:607-619.e15. https://doi.org/10.1016/j.ccell.2018.03.013

53. Zuur AF (2009) Mixed effects models and extensions in ecology with R. Springer, New York, NY

54. Barchetta I, Baroni MG, Melander O, Cavallo MG (2022) New Insights in the Control of Fat Homeostasis: The Role of Neurotensin. IJMS 23:2209. https://doi.org/10.3390/ijms23042209

55. Caldwell A, Coleby R, Tovar C, et al (2018) The newly-arisen Devil facial tumour disease 2 (DFT2) reveals a mechanism for the emergence of a contagious cancer. eLife 7:. https://doi.org/10.7554/eLife.35314

56. Pajak B, Siwiak E, Sołtyka M, et al (2019) 2-Deoxy-d-Glucose and Its Analogs: From Diagnostic to Therapeutic Agents. IJMS 21:234. https://doi.org/10.3390/ijms21010234

57. Weinberg F, Chandel NS (2009) Mitochondrial Metabolism and Cancer. Annals of the New York Academy of Sciences 1177:66–73. https://doi.org/10.1111/j.1749-6632.2009.05039.x

58. Adant I, Bird M, Decru B, et al (2022) Pyruvate and uridine rescue the metabolic profile of OXPHOS dysfunction. Mol Metab 63:101537. https://doi.org/10.1016/j.molmet.2022.101537

59. Liemburg-Apers DC, Willems PHGM, Koopman WJH, Grefte S (2015) Interactions between mitochondrial reactive oxygen species and cellular glucose metabolism. Arch Toxicol 89:1209–1226. https://doi.org/10.1007/s00204-015-1520-y

60. Vishwa R, BharathwajChetty B, Girisa S, et al (2024) Lipid metabolism and its implications in tumor cell plasticity and drug resistance: what we learned thus far? Cancer Metastasis Rev s10555-024-10170–1. https://doi.org/10.1007/s10555-024-10170-1

61. Currie E, Schulze A, Zechner R, et al (2013) Cellular Fatty Acid Metabolism and Cancer. Cell Metabolism 18:153–161. https://doi.org/10.1016/j.cmet.2013.05.017

62. Cheng S, Wang G, Wang Y, et al (2019) Fatty acid oxidation inhibitor etomoxir suppresses tumor progression and induces cell cycle arrest via PPARγ-mediated pathway in bladder cancer. Clinical Science 133:1745–1758. https://doi.org/10.1042/CS20190587

63. TeSlaa T, Ralser M, Fan J, Rabinowitz JD (2023) The pentose phosphate pathway in health and disease. Nat Metab 5:1275–1289. https://doi.org/10.1038/s42255-023-00863-2

64. Hao S, Meng Q, Sun H, et al (2022) The role of transketolase in human cancer progression and therapy. Biomedicine & Pharmacotherapy 154:113607. https://doi.org/10.1016/j.biopha.2022.113607

65. Zhang J, Pavlova NN, Thompson CB (2017) Cancer cell metabolism: the essential role of the nonessential amino acid, glutamine. EMBO J 36:1302–1315. https://doi.org/10.15252/embj.201696151

66. Owen RS, Ramarathinam SH, Bailey A, et al (2021) The differentiation state of the Schwann cell progenitor drives phenotypic variation between two contagious cancers. PLoS Pathog 17:e1010033. https://doi.org/10.1371/journal.ppat.1010033

67. Guo N, Luo Q, Zheng Q, et al (2024) Current status and progress of research on the ADP-dependent glucokinase gene. Front Oncol 14:1358904. https://doi.org/10.3389/fonc.2024.1358904

68. Tanner LB, Goglia AG, Wei MH, et al (2018) Four Key Steps Control Glycolytic Flux in Mammalian Cells. Cell Systems 7:49-62.e8. https://doi.org/10.1016/j.cels.2018.06.003

69. Huang B, Song B, Xu C (2020) Cholesterol metabolism in cancer: mechanisms and therapeutic opportunities. Nat Metab 2:132–141. https://doi.org/10.1038/s42255-020-0174-0

70. Sbodio JI, Snyder SH, Paul BD (2019) Regulators of the transsulfuration pathway. British J Pharmacology 176:583–593. https://doi.org/10.1111/bph.14446

71. Ingles ED, Deakin JE (2015) Global DNA Methylation patterns on marsupial and devil facial tumour chromosomes. Molecular Cytogenetics 8:. https://doi.org/10.1186/s13039-015-0176-x

72. Uchida S, Uchida H, Maruyama T, et al (2013) Molecular Analysis of a Mutated FSH Receptor Detected in a Patient with Spontaneous Ovarian Hyperstimulation Syndrome. PLoS ONE 8:e75478. https://doi.org/10.1371/journal.pone.0075478

73. Dragic H, Chaveroux C, Cosset E, Manie SN (2022) Modelling cancer metabolism *in vitro*: current improvements and future challenges. The FEBS Journal febs.16704. https://doi.org/10.1111/febs.16704

74. Siddle HV, Kaufman J (2013) A tale of two tumours: Comparison of the immune escape strategies of contagious cancers. Molecular Immunology 55:190–193. https://doi.org/10.1016/j.molimm.2012.10.017

75. James S, Jennings G, Kwon YM, et al (2019) Tracing the rise of malignant cell lines: Distribution, epidemiology and evolutionary interactions of two transmissible cancers in Tasmanian devils. Evolutionary Applications 12:1772–1780. https://doi.org/10.1111/eva.12831

76. Maynard Smith J (1978) The evolution of sex. Cambridge University Press, Cambridge [Eng.]; New York

77. Muller HJ (1964) The relation of recombination to mutational advance. Mutation Research/Fundamental and Molecular Mechanisms of Mutagenesis 1:2–9. https://doi.org/10.1016/0027-5107(64)90047-8

78. Bramwell G, DeGregori J, Thomas F, Ujvari B (2024) Transmissible cancers, the genomes that do not melt down. Evolution qpae063. https://doi.org/10.1093/evolut/qpae063

79. Shi DD, Savani MR, Abdullah KG, McBrayer SK (2023) Emerging roles of nucleotide metabolism in cancer. Trends in Cancer 9:624–635. https://doi.org/10.1016/j.trecan.2023.04.008

80. Wang B, Pu R (2023) Association between glycolysis markers and prognosis of liver cancer: a systematic review and meta-analysis. World J Surg Onc 21:390. https://doi.org/10.1186/s12957-023-03275-4

81. Yu M, Chen S, Hong W, et al (2019) Prognostic role of glycolysis for cancer outcome: evidence from 86 studies. J Cancer Res Clin Oncol 145:967–999. https://doi.org/10.1007/s00432-019-02847-w

TABLES

Table 1. Cell lines used in the present study.

Cell line	DFT	Sex of host	Date collected	Location (Tasmania)
4906	DFT1	Male	17/01/2007	Coles Bay
1426	DFT1	Female	10/10/2005	Fentonbury
C5065	DFT1	Unknown	23/07/2007	Bangor
RV	DFT2	Male	26/03/2014	Cygnet
SN	DFT2	Male	12/10/2014	Lower Snug
TD549	DFT2	Male	16/12/2015	Woodbridge

Table 2. Treatment conditions and compositions in the metabolic inhibition experiments.

Treatment	Composition
2DG	2-deoxy-D-glucose 1 mM (Sigma, D8375)
2DG + pyruvate	2-deoxy-D-glucose 1 mM + pyruvate 5 mM (Sigma, P2256)
BPTES	BPTES 5 µM (Sigma, SML0601)
DON	DON 25 µM (Sigma, D2141)
Etomoxir	etomoxir 0.01 mM (Sigma, E1905)
Galactose	RPMI, no glucose (Gibco, 11879020) + galactose 11 mM (Sigma, G5388)
Galactose + pyruvate	RPMI, no glucose + galactose 11 mM + pyruvate 5 mM
Glucose + pyruvate	pyruvate 5 mM
Inhibitor 968	inhibitor 968 25 µM (Sigma, SML1327)
No glucose	RPMI, no glucose
No glutamine	no GlutaMAX
Oxythiamine	oxythiamine 1 mM (Sigma, 0400)
Pioglitazone	pioglitazone hydrochloride 30 µM (Merck, PHR1632)
Oligomycin	oligomycin A 5 µM (Merck, 75351)

Table 3. Key resources used in the study

REAGENT or RESOURCE	SOURCE	IDENTIFIER

Chemicals, peptides, and recombinant proteins		
TRI Reagent®	Sigma	Cat#T9624
2-deoxy-D-glucose	Sigma	Cat#D8375
pyruvate	Sigma	Cat#P2256
BPTES	Sigma	Cat#SML0601
DON	Sigma	Cat#D2141
etomoxir	Sigma	Cat#E1905
galactose	Sigma	Cat#G5388
inhibitor 968	Sigma	Cat#SML1327
oxythiamine	Sigma	Cat#0400
pioglitazone hydrochloride	Merck	Cat#PHR1632
oligomycin A	Merck	Cat#75351
H2DCFDA	Sigma	Cat#D6883
MitoSOX™ Green	Thermo Fisher Scientific	Cat#M36006
chloroform	Merck	Cat#1.02445
isopropanol	Chem Supply	Cat#AH323-4
IGEPAL	Merck	Cat#CA-630
Critical commercial assays		
Zymo Direct-zol™ RNA kit	Zymo Research	Cat#R2051
NEBNext® Ultra™ II Directional RNA Library Prep Kit for Illumina	New England Biolabs	Cat#E7760
Cell Proliferation Kit I	Roche	Cat#11465007001
ATPlite 1step kit Lactate Assay Kit Cholesterol Quantitation Kit	PerkinElmer Sigma Sigma	Cat#6016731 Cat#MAK064 Cat#MAK043
Deposited data		
DFT1 and DFT2 primary tumours RNA sequences	Patchett et al. [26]	http://www.ebi.ac.uk/ena/data/view/PRJEB28680
DFT1 and DFT2 cell line RNA sequences	This paper	https://www.ncbi.nlm.nih.gov/bioproject/PRJNA1122388/
DFT1 and DFT2 cell line RNA untransformed count matrix	This paper	https://github.com/Anne-LiseGerard/dftd_rnaseq/
Tasmanian devil reference genome mSarHar1.11	Stammnitz et al. [22]	https://ftp.ensembl.org/pub/release-109/fasta/sarcophilus_harrisii/
Reactome	Gillespie et al. [46]	https://reactome.org
Experimental models: Cell lines		
4906 (DFT1)	Pyecroft et al. [31]	N/A
C5065 (DFT1)	Pyecroft et al. [31]	N/A
1426 (DFT1)	Pyecroft et al. [31]	N/A

RV (DFT2)	Pye et al. [21]	N/A
SN (DFT2) TD549 (DFT2)	Pye et al. [21] Pye et al. [21]	N/A N/A
Software and algorithms		
skewer	Jiang et al. [39]	https://github.com/relipmoc/skewer
kallisto	Bray et al. [40]	https://github.com/pachterlab/kallisto
Bash	GNU[41]	https://www.gnu.org/software/bash/
BioMart	Smedley et al. [42]	https://asia.ensembl.org/info/data/biomart/index.html
DESeq2	Love et al. [43]	https://bioconductor.org/packages/release/bioc/html/DESeq2.html
mitch	Kaspi and Ziemann [45]	https://www.bioconductor.org/packages/release/bioc/html/mitch.html
R	R Core Team [47]	https://www.r-project.org
STAR	Dobin et al. [48]	https://github.com/alexdobin/STAR
SAMtools BEDtools	Li et al. [49] Quinlan and Hall [50]	http://www.htslib.org https://bedtools.readthedocs.io/en/latest/
Other		
R scripts	This paper	https://github.com/Anne-LiseGerard/dftd_rnaseq/
Bash scripts	This paper	https://github.com/Anne-LiseGerard/dftd_rnaseq/

SUPPORTING INFORMATION

Figure S1. Multi-contrast pathway enrichment analysis using mitch.

Table S1. Tumour purity results.

Table S2. Gene list summary.

Table S3. Mixed effects model selection.

Table S4. Mixed effects models outputs.

FIGURE LEGENDS

Figure 1 *In vitro* Devil Facial Tumour 1 (DFT1) and DFT2 transcriptomes differ more than *in vivo* ones. **A** Multi-dimensional scaling (MDS) plot of biopsy RNA sequences (Devil Facial Tumour 1, DFT1 in blue triangles and DFT2 in pink triangles). One experiment, 8 samples, 2 biological replicates per DFT, 2 technical replicates per biological replicate. **B** MDS plot of cell line RNA sequences (DFT1 in blue circles and DFT2 in pink circles). One experiment, 18 samples, 3 biological replicates per DFT, 3 technical replicates per biological replicate. **C** MDS plot of both cell line and biopsy RNA sequences. **D** Top 20 genes up- and top 20 genes down-regulated in DFT2, for biopsies and cell lines. **E** Multi-contrast enrichment analysis results. Each dot represents one gene set and is plotted according to its enrichment score (s) within the cell line dataset and the biopsy dataset. Significantly enriched (False Discovery Rate < 0.05) gene sets are shown in red.

Figure 2 Cholesterol biosynthesis and nucleotide metabolism show concordant enrichment in Devil Facial Tumour 2 (DFT2). **A** Multi-contrast pathway analysis performed with mitch on Reactome pathways, filtered for metabolism-related gene sets with an adjusted pvalue < 0.05. Each circle or triangle represents one gene set and is plotted according to its enrichment score (s-dist). Triangle or circle size is scaled according to the number of genes in a pathway (set size). Heatmaps of Differentially Expressed genes (DEGs) for **B** cholesterol biosynthesis genes, **C** nucleotide metabolism genes and **D** sulfur amino acid metabolism genes. Only significant DEGs are represented (False Discovery Rate < 0.05).

Figure 3 Devil Facial Tumour 2 (DFT2) cells show higher glycolysis rates than DFT1 cells. **A** Lactate quantity measured in cell culture supernatant, best fit model: lactate ~ cell line + day. Two independent experiments were performed, each comprised duplicates for each cell line. **B** Total (glucose), oxidative (2-deoxy-D-glucose, 2DG) and glycolytic (oligomycin) adenosine triphosphate (ATP) production. Best fit model: ATP ~ treatment * cell line + (1 | experiment). Three independent experiments were performed, each comprised of 6 technical replicates per cell line. **C** Percent viability of Devil Facial Tumour 1 (DFT1, blue) and DFT2 (red) cell lines grown in treatments targeting glucose metabolism relative to glucose control medium. Best fit model: % viability ~ treatment * cell line + (1 | experiment). Three

independent experiments were performed; each comprised 6 technical replicates per cell line. **A**, **B** and **C** Mean and 95 % confidence intervals shown in colour and data points in grey. Compact letter display represents post hoc contrasts for which $p < 0.05$. Following Tukey's post hoc test (with Bonferroni correction) each group was assigned a letter. Groups that share a letter are not significantly different from each other. Groups with different letters are significantly different at a threshold of $p < 0.05$. **D** Heatmaps of DEGs for glycolysis genes. Only significant DEGs are represented (False Discovery Rate < 0.05).

Figure 4 Devil Facial Tumour 2 (DFT2) cells produce more reactive oxygen species (ROS) than DFT1 cells. **A** Overall ROS and **B** mitochondrial ROS production in relative fluorescence units (RFU) of DFT1 and DFT2 cell lines after 1 hour. Best fit model: ROS ~ cell line. Three independent experiments were performed; each comprised 6 technical replicates per cell line. Mean and 95 % confidence intervals shown in colour and data points in grey. Compact letter display represents post hoc contrasts for which $p < 0.05$. Following Tukey's post hoc test (with Bonferroni correction) each group was assigned a letter. Groups that share a letter are not significantly different from each other. Groups with different letters are significantly different at a threshold of $p < 0.05$. **C** Heatmaps of differentially expressed genes (DEGs) for ROS detoxification genes. Only significant DEGs are represented (False Discovery Rate < 0.05).

Figure 5 Devil Facial Tumour 2 (DFT2) relies more on lipid metabolism than DFT1, and other pathways of interest. Percent viability of DFT1 (blue) and DFT2 (red) cell lines grown in treatments targeting **A** fatty acid oxidation and the pentose phosphate pathway (PPP) and **B** fatty acid oxidation and oxidative phosphorylation (OXPHOS). **C** Heatmaps of differentially expressed genes (DEGs) for fatty acid metabolism. Only significant DEGs are represented (False Discovery Rate < 0.05). **D** Cholesterol content of lipids extracted from 10^6 cells, best fit model: cholesterol ~ DFT. Three samples per cell line, each from independent cell subcultures, were used for this experiment. **E** Percent viability of DFT1 and DFT2 cell lines grown in treatments targeting glutamine metabolism. **A**, **B** and **E** Three independent experiments were performed; each comprised 6 technical replicates per cell line. Best fit models: % viability ~ treatment * cell line. **A**, **B**, **D** and **E** Mean and 95 % confidence intervals shown in colour and data points in grey. Compact letter display represents post hoc contrasts for which $p < 0.05$. Following Tukey's post hoc test (with Bonferroni correction) each group was assigned a letter. Groups that share a letter are not significantly different from each other. Groups with different letters are significantly different at a threshold of $p < 0.05$.

Fig.1. A

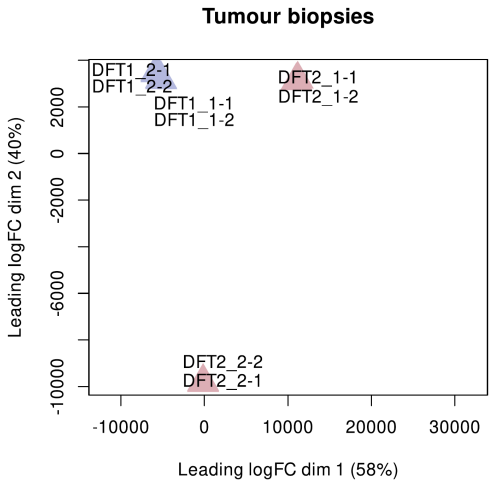

B

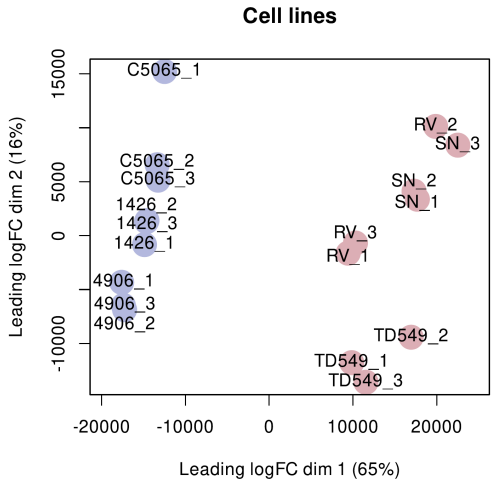

C

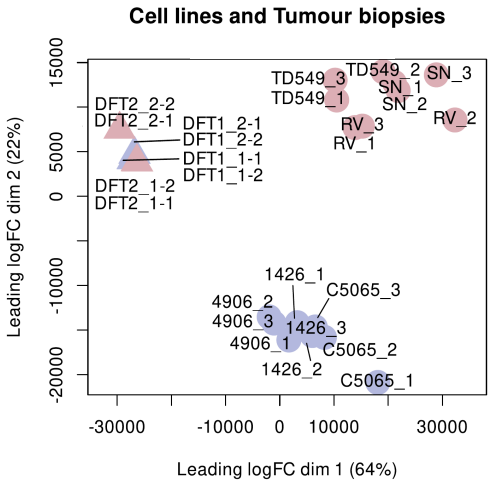

D

Top 40 DEGs

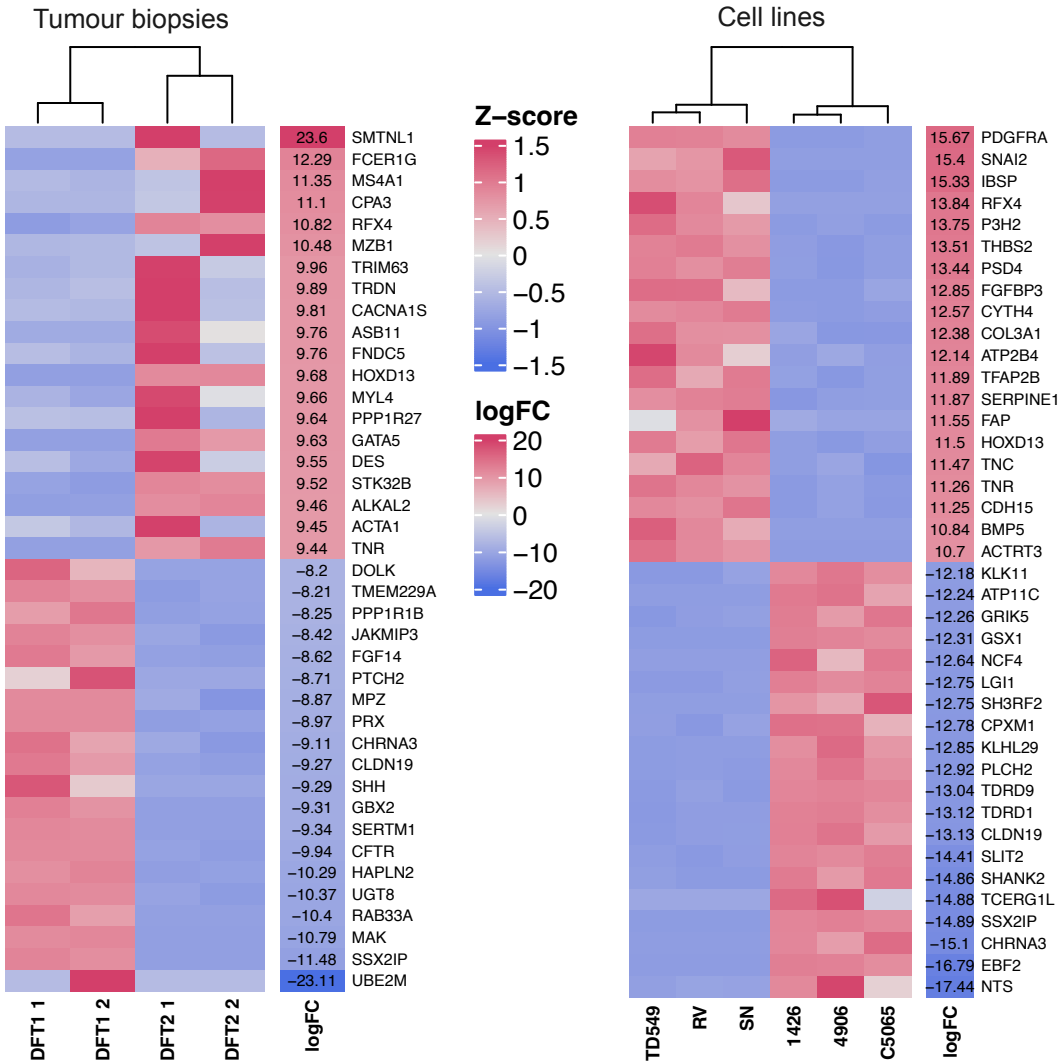

E

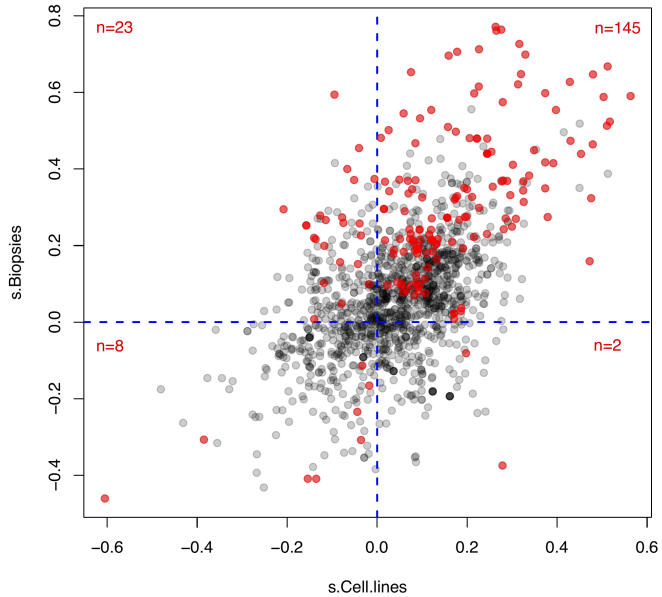

Fig. 2. A

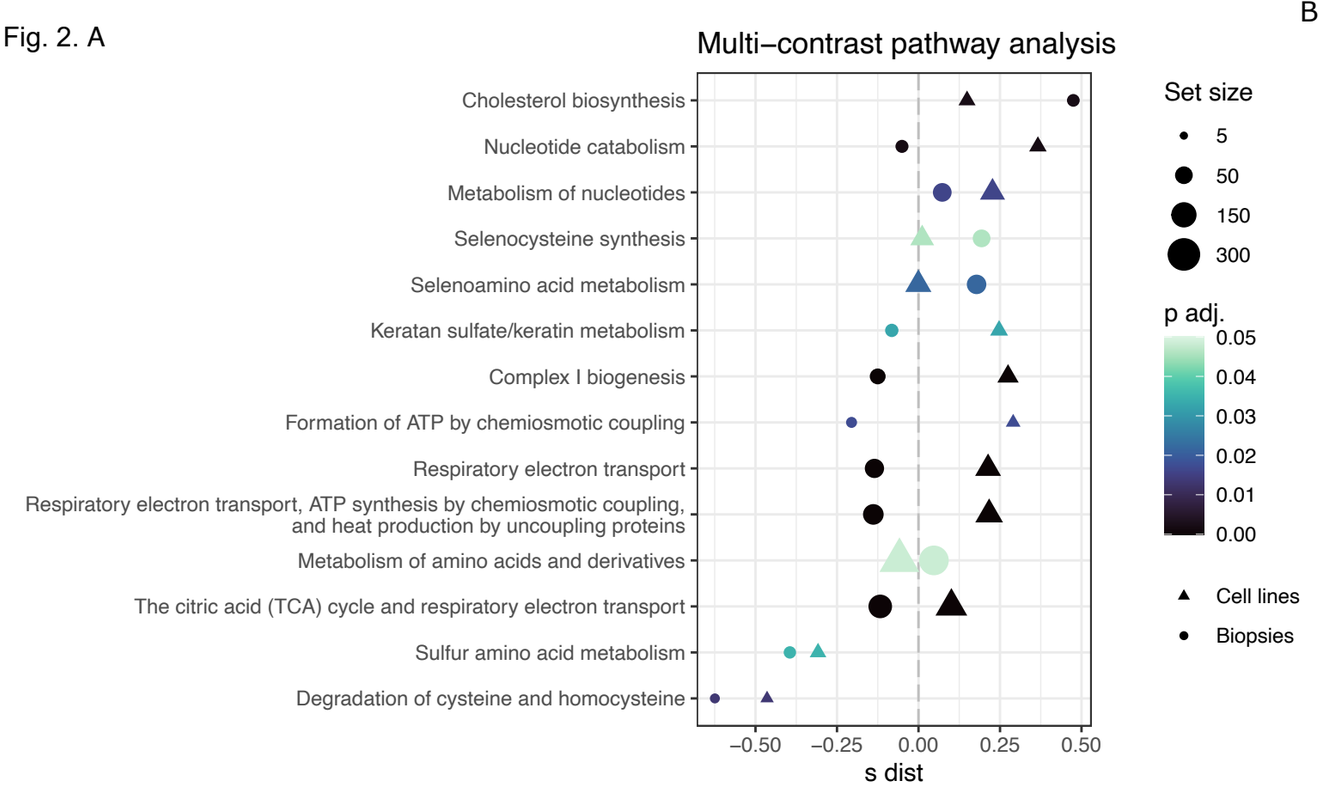
Multi−contrast pathway analysis
Cholesterol biosynthesis
Nucleotide catabolism
Metabolism of nucleotides
Selenocysteine synthesis
Selenoamino acid metabolism
Keratan sulfate/keratin metabolism
Complex I biogenesis
Formation of ATP by chemiosmotic coupling
Respiratory electron transport
Respiratory electron transport, ATP synthesis by chemiosmotic coupling, and heat production by uncoupling proteins
Metabolism of amino acids and derivatives
The citric acid (TCA) cycle and respiratory electron transport
Sulfur amino acid metabolism
Degradation of cysteine and homocysteine
−0.50
−0.25
0.00
0.25
0.50
s dist
Set size
5
50
150
300
p adj.
0.05
0.04
0.03
0.02
0.01
0.00
Cell lines
Biopsies

B

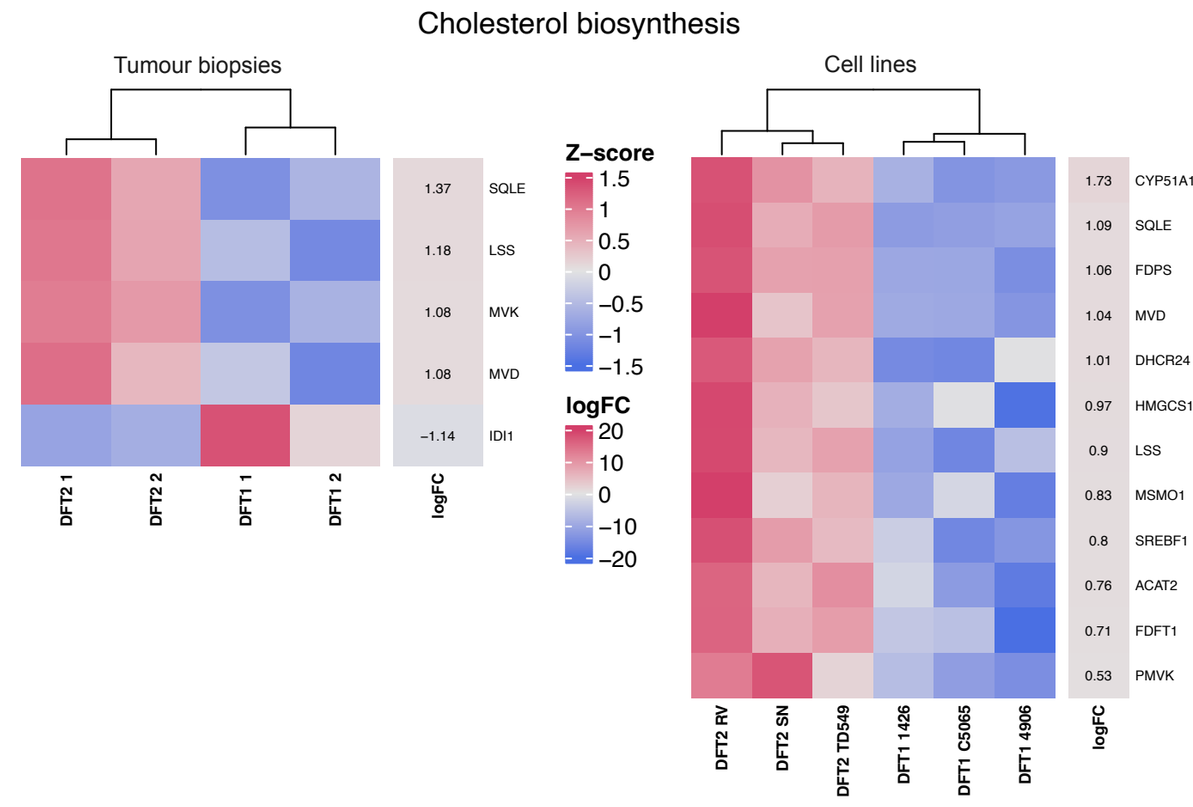
Cholesterol biosynthesis
Tumour biopsies
Cell lines
Z−score
1.5
1
0.5
0
−0.5
−1
−1.5
logFC
20
10
0
−10
−20
1.37 SQLE
1.18 LSS
1.08 MVK
1.08 MVD
−1.14 IDI1
DFT2 1
DFT2 2
DFT1 1
DFT1 2
logFC
1.73 CYP51A1
1.09 SQLE
1.06 FDPS
1.04 MVD
1.01 DHCR24
0.97 HMGCS1
0.9 LSS
0.83 MSMO1
0.8 SREBF1
0.76 ACAT2
0.71 FDFT1
0.53 PMVK
DFT2 RV
DFT2 SN
DFT2 TD549
DFT1 1426
DFT1 C5065
DFT1 4906
logFC

C

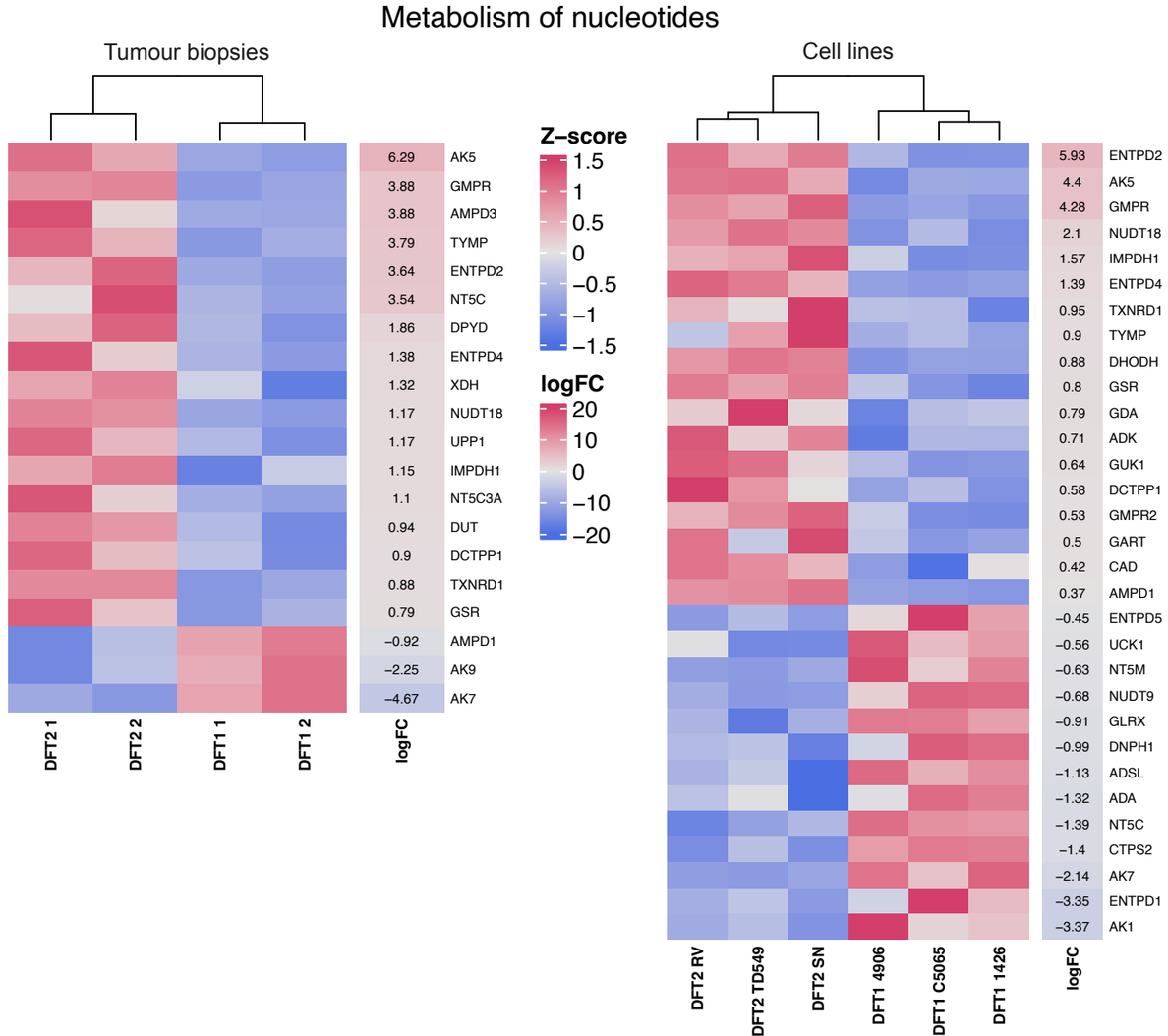
Metabolism of nucleotides
Tumour biopsies
Cell lines
Z−score
1.5
1
0.5
0
−0.5
−1
−1.5
logFC
20
10
0
−10
−20
6.29 AK5
3.88 GMPR
3.88 AMPD3
3.79 TYMP
3.64 ENTPD2
3.54 NT5C
1.86 DPYD
1.38 ENTPD4
1.32 XDH
1.17 NUDT18
1.17 UPP1
1.15 IMPDH1
1.1 NT5C3A
0.94 DUT
0.9 DCTPP1
0.88 TXNRD1
0.79 GSR
−0.92 AMPD1
−2.25 AK9
−4.67 AK7
DFT2 1
DFT2 2
DFT1 1
DFT1 2
logFC
5.93 ENTPD2
4.4 AK5
4.28 GMPR
2.1 NUDT18
1.57 IMPDH1
1.39 ENTPD4
0.95 TXNRD1
0.9 TYMP
0.88 DHODH
0.8 GSR
0.79 GDA
0.71 ADK
0.64 GUK1
0.58 DCTPP1
0.53 GMPR2
0.5 GART
0.42 CAD
0.37 AMPD1
−0.45 ENTPD5
−0.56 UCK1
−0.63 NT5M
−0.68 NUDT9
−0.91 GLRX
−0.99 DNPH1
−1.13 ADSL
−1.32 ADA
−1.39 NT5C
−1.4 CTPS2
−2.14 AK7
−3.35 ENTPD1
−3.37 AK1
DFT2 RV
DFT2 TD549
DFT2 SN
DFT1 4906
DFT1 C5065
DFT1 1426
logFC

D

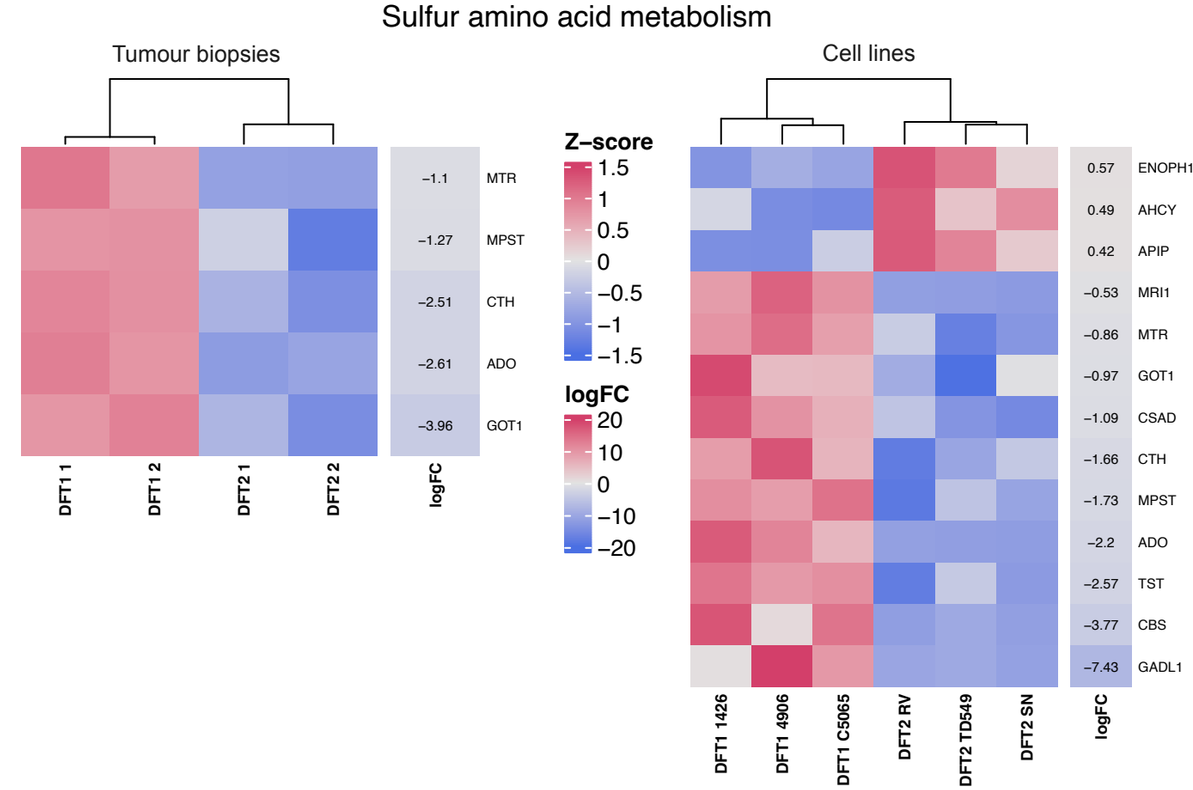
Sulfur amino acid metabolism
Tumour biopsies
Cell lines
Z−score
1.5
1
0.5
0
−0.5
−1
−1.5
logFC
20
10
0
−10
−20
−1.1 MTR
−1.27 MPST
−2.51 CTH
−2.61 ADO
−3.96 GOT1
DFT1 1
DFT1 2
DFT2 1
DFT2 2
logFC
0.57 ENOPH1
0.49 AHCY
0.42 APIP
−0.53 MRI1
−0.86 MTR
−0.97 GOT1
−1.09 CSAD
−1.66 CTH
−1.73 MPST
−2.2 ADO
−2.57 TST
−3.77 CBS
−7.43 GADL1
DFT1 1426
DFT1 4906
DFT1 C5065
DFT2 RV
DFT2 TD549
DFT2 SN
logFC

Fig. 3. A

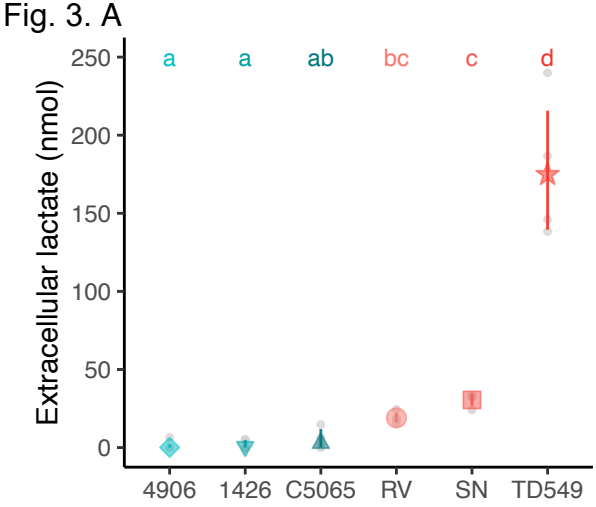
Extracellular lactate (nmol)
250
200
150
100
50
0
a
a
ab
bc
c
d
4906
1426
C5065
RV
SN
TD549

B

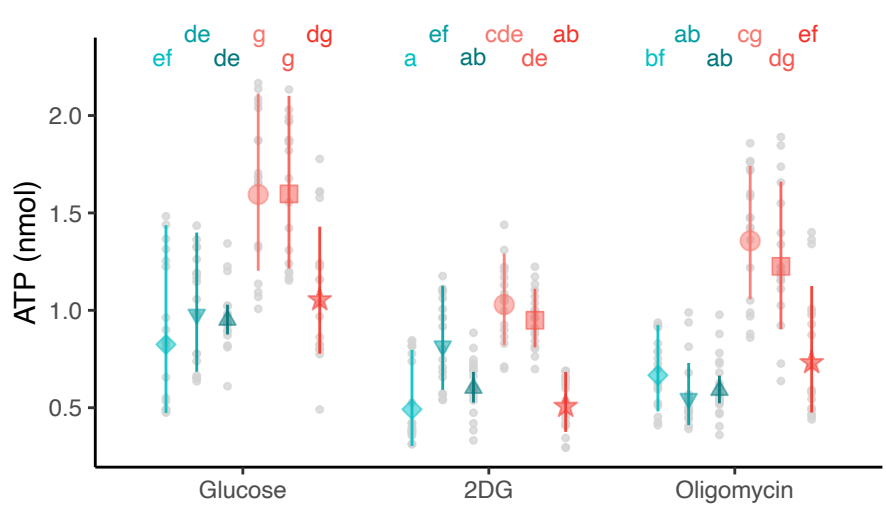
ATP (nmol)
2.0
1.5
1.0
0.5
ef de g dg
ef de g
a ef ab cde de ab
bf ab ab cg dg ef
Glucose
2DG
Oligomycin

C

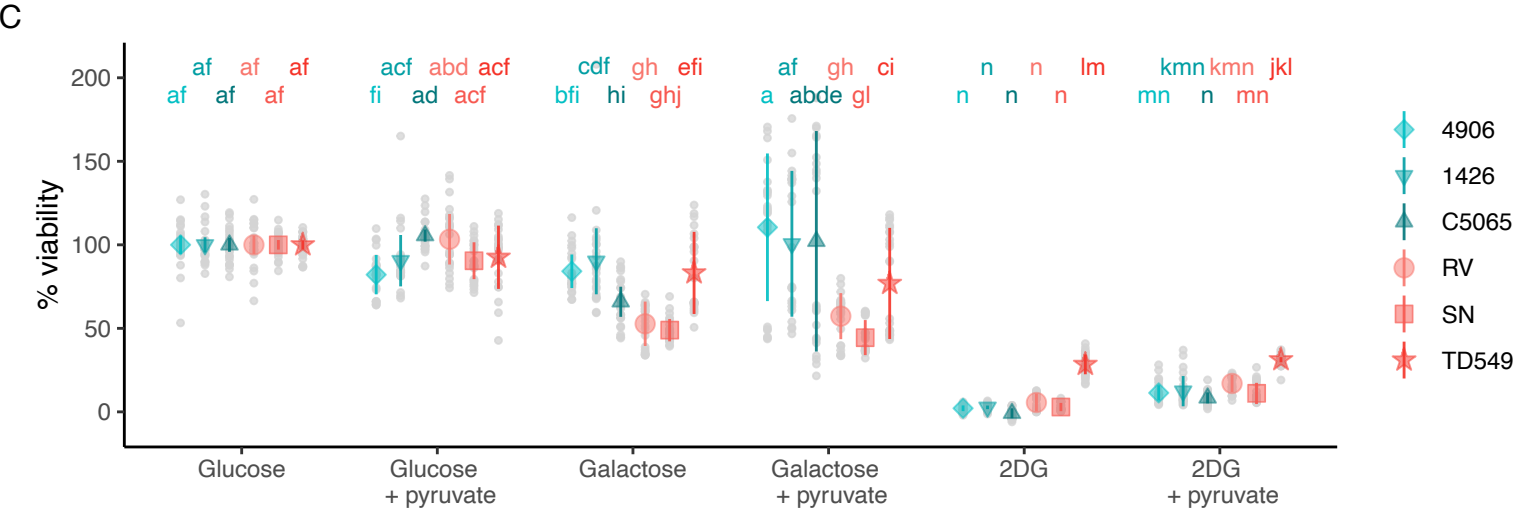
% viability
200
150
100
50
0
af af af
af af af
acf abd acf
fi ad acf
cdf gh efi
bfi hi ghj
af gh ci
a abde gl
n n lm
n n n
kmn kmn jkl
mn n mn
Glucose
Glucose + pyruvate
Galactose
Galactose + pyruvate
2DG
2DG + pyruvate
4906
1426
C5065
RV
SN
TD549

D

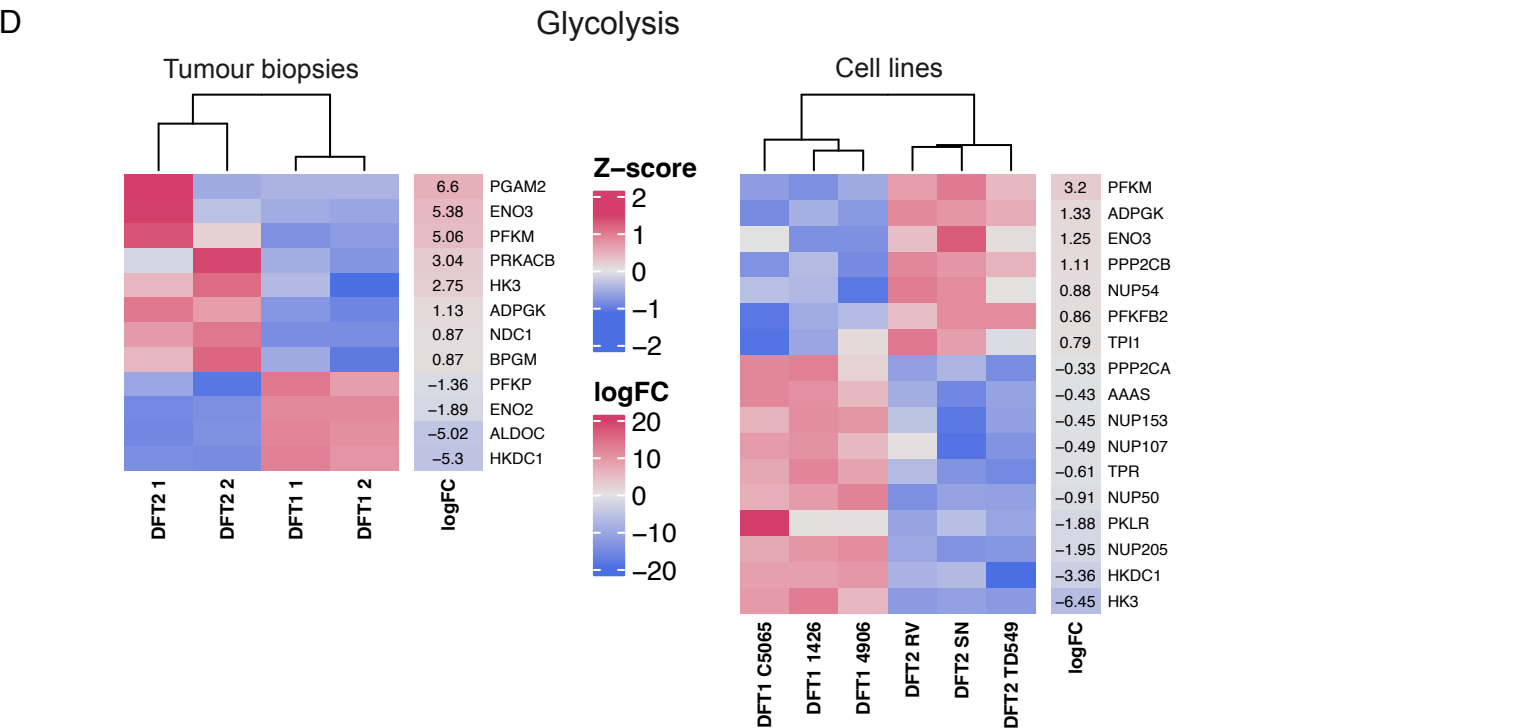
Glycolysis
Tumour biopsies
Cell lines
Z-score
2
1
0
−1
−2
logFC
20
10
0
−10
−20
6.6 PGAM2
5.38 ENO3
5.06 PFKM
3.04 PRKACB
2.75 HK3
1.13 ADPGK
0.87 NDC1
0.87 BPGM
−1.36 PFKP
−1.89 ENO2
−5.02 ALDOC
−5.3 HKDC1
DFT2 1
DFT2 2
DFT1 1
DFT1 2
logFC
3.2 PFKM
1.33 ADPGK
1.25 ENO3
1.11 PPP2CB
0.88 NUP54
0.86 PFKFB2
0.79 TPI1
−0.33 PPP2CA
−0.43 AAAS
−0.45 NUP153
−0.49 NUP107
−0.61 TPR
−0.91 NUP50
−1.88 PKLR
−1.95 NUP205
−3.36 HKDC1
−6.45 HK3
DFT1 C5065
DFT1 1426
DFT1 4906
DFT2 RV
DFT2 SN
DFT2 TD549
logFC

Fig. 4. A

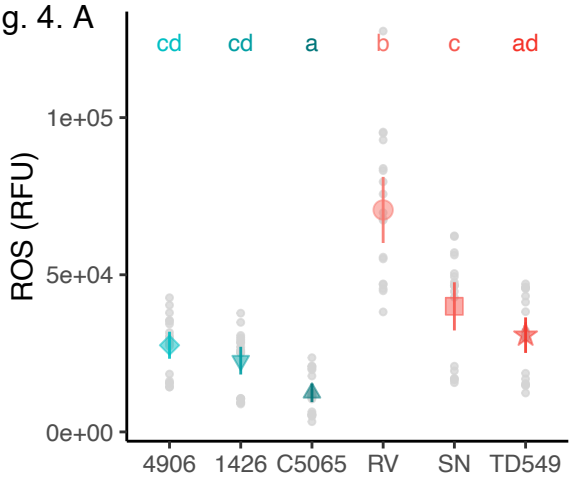
cd
cd
a
b
c
ad
ROS (RFU)
1e+05
5e+04
0e+00
4906
1426
C5065
RV
SN
TD549

B

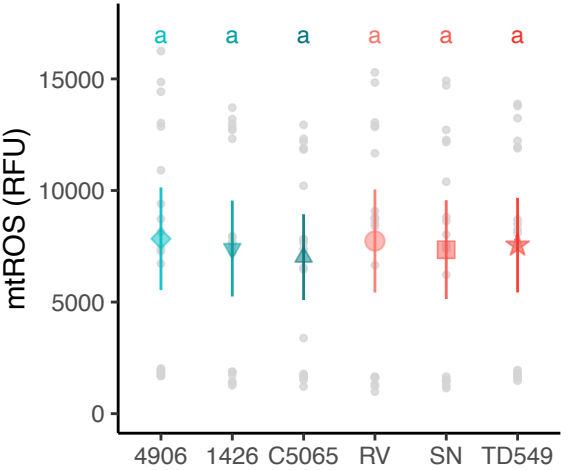
a
a
a
a
a
a
mtROS (RFU)
15000
10000
5000
0
4906
1426
C5065
RV
SN
TD549

C

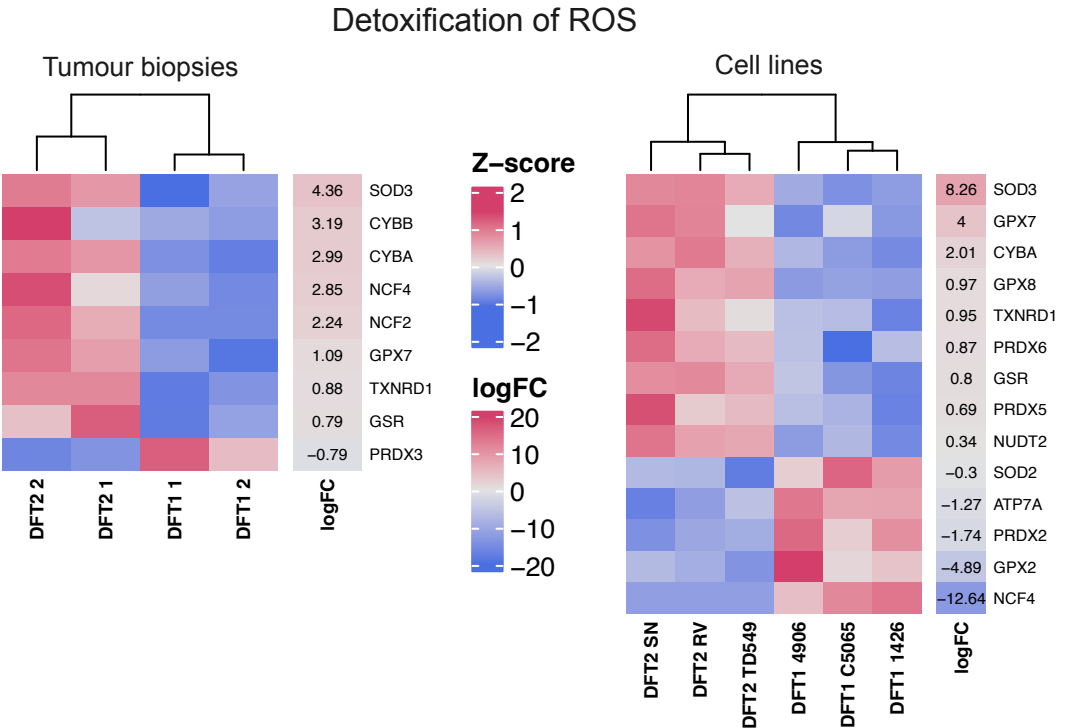
Detoxification of ROS
Tumour biopsies
Cell lines
Z–score
2
1
0
−1
−2
logFC
20
10
0
−10
−20
4.36 SOD3
3.19 CYBB
2.99 CYBA
2.85 NCF4
2.24 NCF2
1.09 GPX7
0.88 TXNRD1
0.79 GSR
−0.79 PRDX3
DFT2 2
DFT2 1
DFT1 1
DFT1 2
logFC
8.26 SOD3
4 GPX7
2.01 CYBA
0.97 GPX8
0.95 TXNRD1
0.87 PRDX6
0.8 GSR
0.69 PRDX5
0.34 NUDT2
−0.3 SOD2
−1.27 ATP7A
−1.74 PRDX2
−4.89 GPX2
−12.64 NCF4
DFT2 SN
DFT2 RV
DFT2 TD549
DFT1 4906
DFT1 C5065
DFT1 1426
logFC

Fig. 5. A

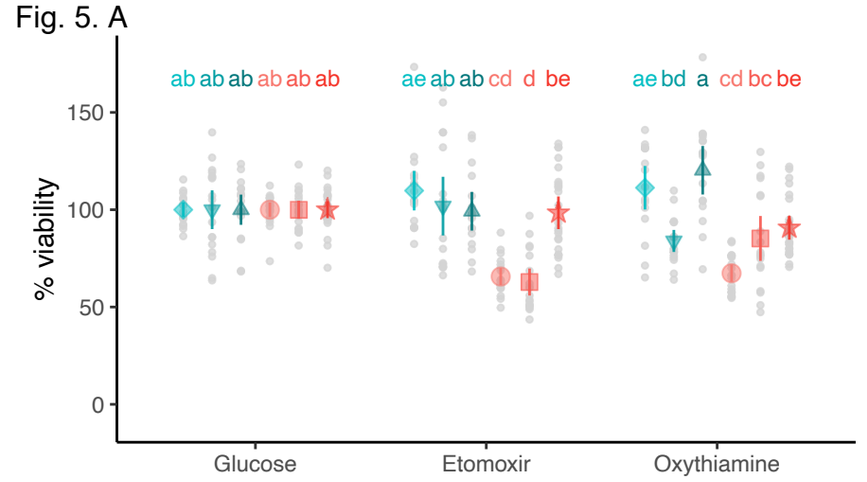
ab ab ab ab ab ab
ae ab ab cd d be
ae bd a cd bc be
% viability
150
100
50
0
Glucose
Etomoxir
Oxythiamine

B

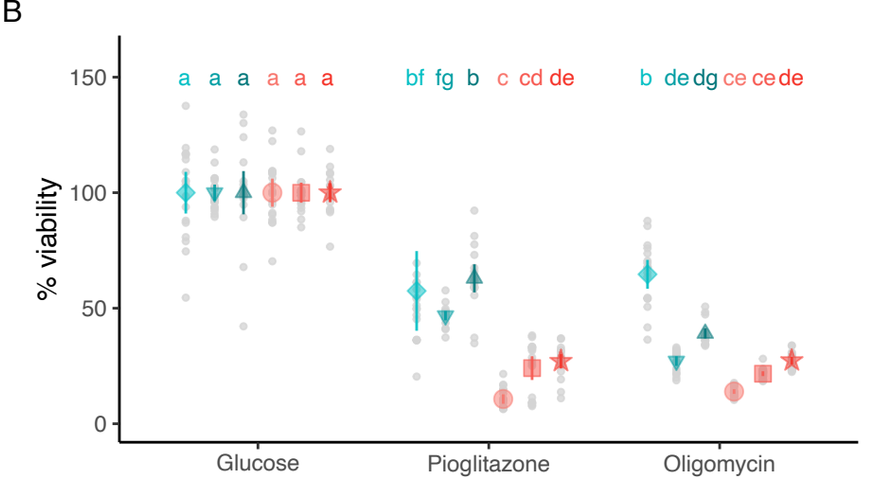
a a a a a a
bf fg b c cd de
b de dg ce ce de
% viability
150
100
50
0
Glucose
Pioglitazone
Oligomycin

C

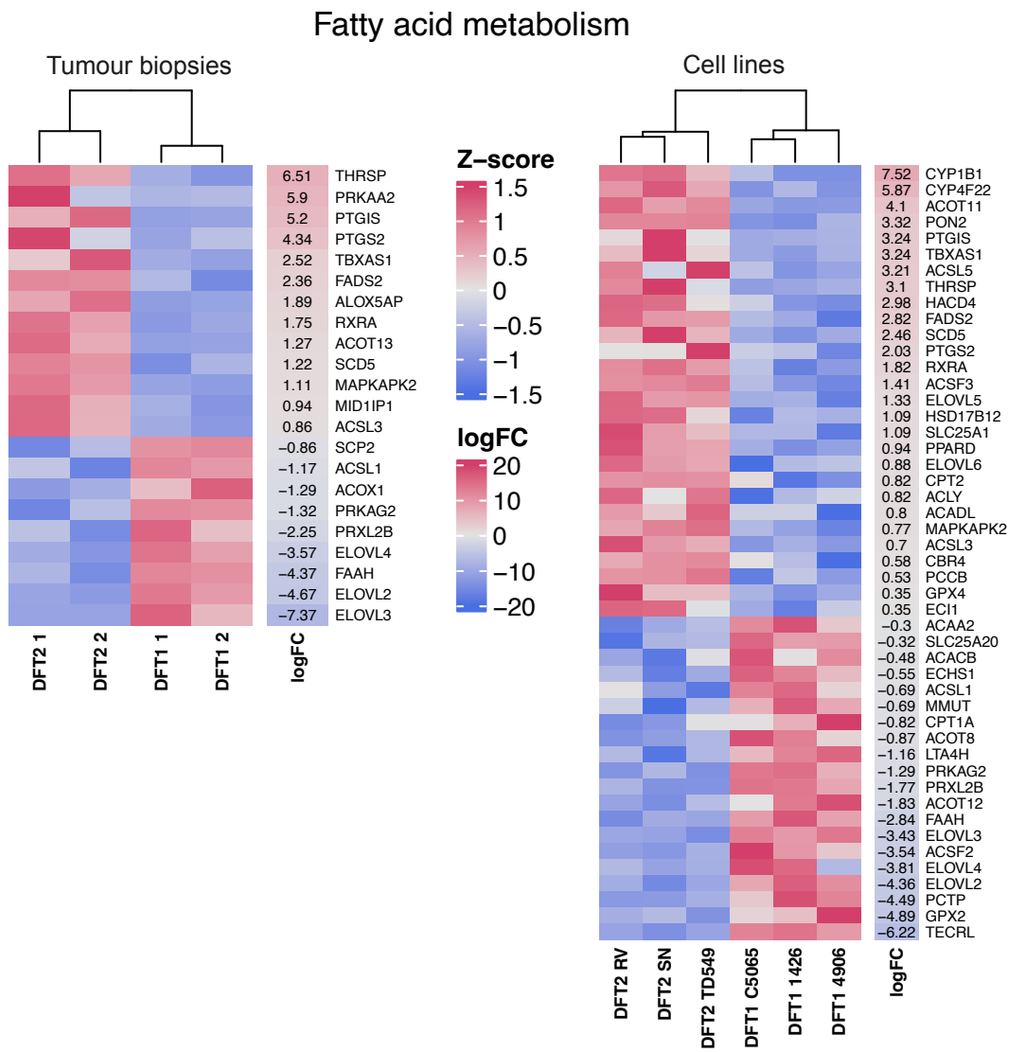
Fatty acid metabolism
Tumour biopsies
Cell lines
Z–score
1.5
1
0.5
0
−0.5
−1
−1.5
logFC
20
10
0
−10
−20
6.51 THRSP
5.9 PRKAA2
5.2 PTGIS
4.34 PTGS2
2.52 TBXAS1
2.36 FADS2
1.89 ALOX5AP
1.75 RXRA
1.27 ACOT13
1.22 SCD5
1.11 MAPKAPK2
0.94 MID1IP1
0.86 ACSL3
−0.86 SCP2
−1.17 ACSL1
−1.29 ACOX1
−1.32 PRKAG2
−2.25 PRXL2B
−3.57 ELOVL4
−4.37 FAAH
−4.67 ELOVL2
−7.37 ELOVL3
DFT2 1
DFT2 2
DFT1 1
DFT1 2
logFC
7.52 CYP1B1
5.87 CYP4F22
4.1 ACOT11
3.32 PON2
3.24 PTGIS
3.24 TBXAS1
3.21 ACSL5
3.1 THRSP
2.98 HACD4
2.82 FADS2
2.46 SCD5
2.03 PTGS2
1.82 RXRA
1.41 ACSF3
1.33 ELOVL5
1.09 HSD17B12
1.09 SLC25A1
0.94 PPARD
0.88 ELOVL6
0.82 CPT2
0.82 ACLY
0.8 ACADL
0.77 MAPKAPK2
0.7 ACSL3
0.58 CBR4
0.53 PCCB
0.35 GPX4
0.35 ECI1
−0.3 ACAA2
−0.32 SLC25A20
−0.48 ACACB
−0.55 ECHS1
−0.69 ACSL1
−0.69 MMUT
−0.82 CPT1A
−0.87 ACOT8
−1.16 LTA4H
−1.29 PRKAG2
−1.77 PRXL2B
−1.83 ACOT12
−2.84 FAAH
−3.43 ELOVL3
−3.54 ACSF2
−3.81 ELOVL4
−4.36 ELOVL2
−4.49 PCTP
−4.89 GPX2
−6.22 TECRL
DFT2 RV
DFT2 SN
DFT2 TD549
DFT1 C5065
DFT1 1426
DFT1 4906
logFC

D

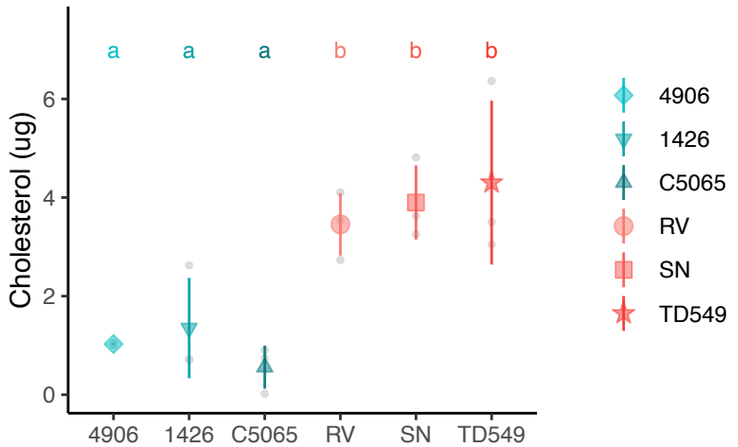
a a a b b b
Cholesterol (ug)
6
4
2
0
4906
1426
C5065
RV
SN
TD549
4906
1426
C5065
RV
SN
TD549

E

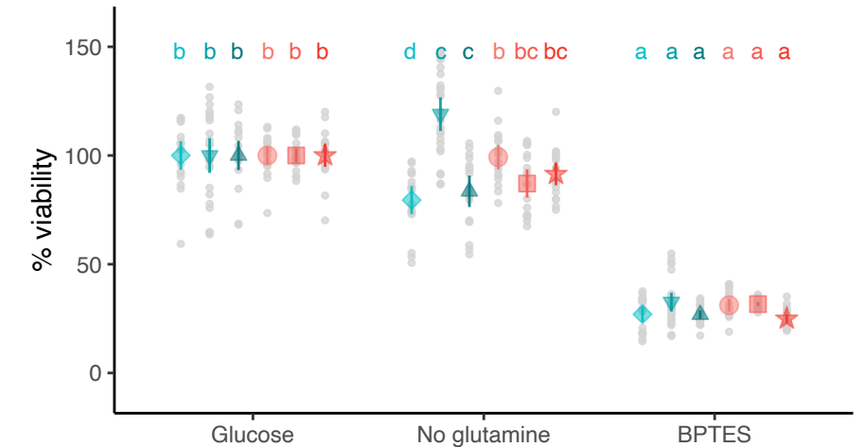
b b b b b b
d c c b bc bc
a a a a a a
% viability
150
100
50
0
Glucose
No glutamine
BPTES

FigS1.

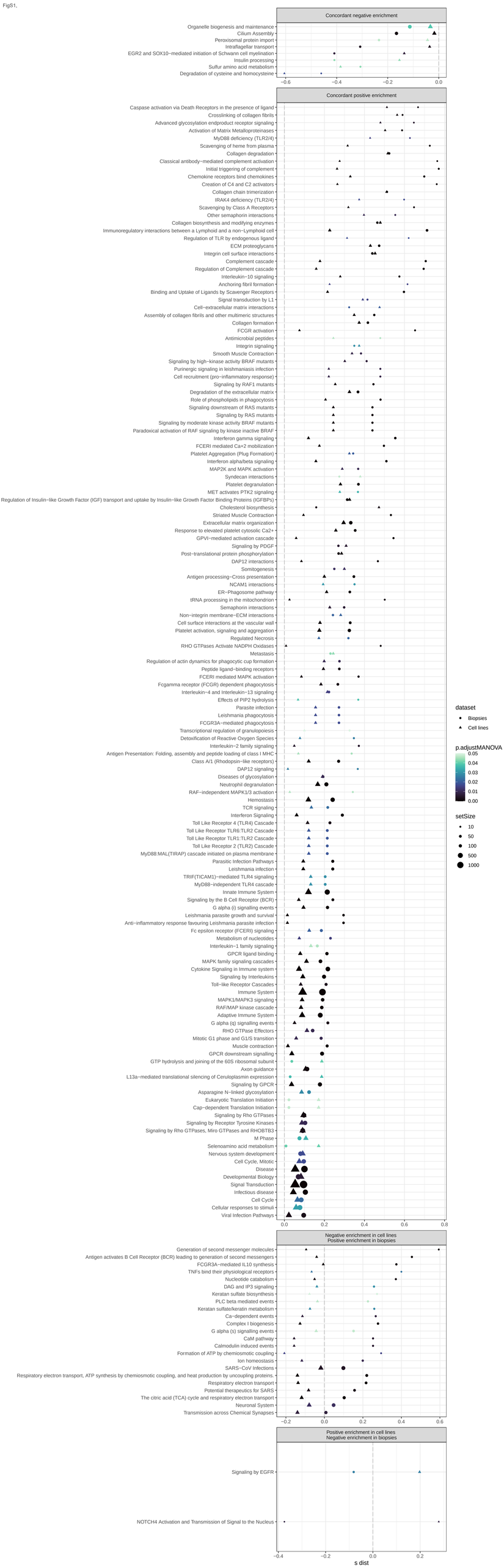
Concordant negative enrichment
Organelle biogenesis and maintenance
Cilium Assembly
Peroxisomal protein import
Intraflagellar transport
EGR2 and SOX10−mediated initiation of Schwann cell myelination
Insulin processing
Sulfur amino acid metabolism
Degradation of cysteine and homocysteine
−0.6
−0.4
−0.2
0.0
Concordant positive enrichment
Caspase activation via Death Receptors in the presence of ligand
Crosslinking of collagen fibrils
Advanced glycosylation endproduct receptor signaling
Activation of Matrix Metalloproteinases
MyD88 deficiency (TLR2/4)
Scavenging of heme from plasma
Collagen degradation
Classical antibody−mediated complement activation
Initial triggering of complement
Chemokine receptors bind chemokines
Creation of C4 and C2 activators
Collagen chain trimerization
IRAK4 deficiency (TLR2/4)
Scavenging by Class A Receptors
Other semaphorin interactions
Collagen biosynthesis and modifying enzymes
Immunoregulatory interactions between a Lymphoid and a non−Lymphoid cell
Regulation of TLR by endogenous ligand
ECM proteoglycans
Integrin cell surface interactions
Complement cascade
Regulation of Complement cascade
Interleukin−10 signaling
Anchoring fibril formation
Binding and Uptake of Ligands by Scavenger Receptors
Signal transduction by L1
Cell−extracellular matrix interactions
Assembly of collagen fibrils and other multimeric structures
Collagen formation
FCGR activation
Antimicrobial peptides
Integrin signaling
Smooth Muscle Contraction
Signaling by high−kinase activity BRAF mutants
Purinergic signaling in leishmaniasis infection
Cell recruitment (pro−inflammatory response)
Signaling by RAF1 mutants
Degradation of the extracellular matrix
Role of phospholipids in phagocytosis
Signaling downstream of RAS mutants
Signaling by RAS mutants
Signaling by moderate kinase activity BRAF mutants
Paradoxical activation of RAF signaling by kinase inactive BRAF
Interferon gamma signaling
FCERI mediated Ca+2 mobilization
Platelet Aggregation (Plug Formation)
Interferon alpha/beta signaling
MAP2K and MAPK activation
Syndecan interactions
Platelet degranulation
MET activates PTK2 signaling
Regulation of Insulin−like Growth Factor (IGF) transport and uptake by Insulin−like Growth Factor Binding Proteins (IGFBPs)
Cholesterol biosynthesis
Striated Muscle Contraction
Extracellular matrix organization
Response to elevated platelet cytosolic Ca2+
GPVI−mediated activation cascade
Signaling by PDGF
Post−translational protein phosphorylation
DAP12 interactions
Somitogenesis
Antigen processing−Cross presentation
NCAM1 interactions
ER−Phagosome pathway
tRNA processing in the mitochondrion
Semaphorin interactions
Non−integrin membrane−ECM interactions
Cell surface interactions at the vascular wall
Platelet activation, signaling and aggregation
Regulated Necrosis
RHO GTPases Activate NADPH Oxidases
Metastasis
Regulation of actin dynamics for phagocytic cup formation
Peptide ligand−binding receptors
FCERI mediated MAPK activation
Fcgamma receptor (FCGR) dependent phagocytosis
Interleukin−4 and Interleukin−13 signaling
Effects of PIP2 hydrolysis
Parasite infection
Leishmania phagocytosis
FCGR3A−mediated phagocytosis
Transcriptional regulation of granulopoiesis
Detoxification of Reactive Oxygen Species
Interleukin−2 family signaling
Antigen Presentation: Folding, assembly and peptide loading of class I MHC
Class A/1 (Rhodopsin−like receptors)
DAP12 signaling
Diseases of glycosylation
Neutrophil degranulation
RAF−independent MAPK1/3 activation
Hemostasis
TCR signaling
Interferon Signaling
Toll Like Receptor 4 (TLR4) Cascade
Toll Like Receptor TLR6:TLR2 Cascade
Toll Like Receptor TLR1:TLR2 Cascade
Toll Like Receptor 2 (TLR2) Cascade
MyD88:MAL(TIRAP) cascade initiated on plasma membrane
Parasitic Infection Pathways
Leishmania infection
TRIF(TICAM1)−mediated TLR4 signaling
MyD88−independent TLR4 cascade
Innate Immune System
Signaling by the B Cell Receptor (BCR)
G alpha (i) signalling events
Leishmania parasite growth and survival
Anti−inflammatory response favouring Leishmania parasite infection
Fc epsilon receptor (FCERI) signaling
Metabolism of nucleotides
Interleukin−1 family signaling
GPCR ligand binding
MAPK family signaling cascades
Cytokine Signaling in Immune system
Signaling by Interleukins
Toll−like Receptor Cascades
Immune System
MAPK1/MAPK3 signaling
RAF/MAP kinase cascade
Adaptive Immune System
G alpha (q) signalling events
RHO GTPase Effectors
Mitotic G1 phase and G1/S transition
Muscle contraction
GPCR downstream signalling
GTP hydrolysis and joining of the 60S ribosomal subunit
Axon guidance
L13a−mediated translational silencing of Ceruloplasmin expression
Signaling by GPCR
Asparagine N−linked glycosylation
Eukaryotic Translation Initiation
Cap−dependent Translation Initiation
Signaling by Rho GTPases
Signaling by Receptor Tyrosine Kinases
Signaling by Rho GTPases, Miro GTPases and RHOBTB3
M Phase
Selenoamino acid metabolism
Nervous system development
Cell Cycle, Mitotic
Disease
Developmental Biology
Signal Transduction
Infectious disease
Cell Cycle
Cellular responses to stimuli
Viral Infection Pathways
0.0
0.2
0.4
0.6
0.8
Negative enrichment in cell lines
Positive enrichment in biopsies
Generation of second messenger molecules
Antigen activates B Cell Receptor (BCR) leading to generation of second messengers
FCGR3A−mediated IL10 synthesis
TNFs bind their physiological receptors
Nucleotide catabolism
DAG and IP3 signaling
Keratan sulfate biosynthesis
PLC beta mediated events
Keratan sulfate/keratin metabolism
Ca−dependent events
Complex I biogenesis
G alpha (s) signalling events
CaM pathway
Calmodulin induced events
Formation of ATP by chemiosmotic coupling
Ion homeostasis
SARS−CoV Infections
Respiratory electron transport, ATP synthesis by chemiosmotic coupling, and heat production by uncoupling proteins.
Respiratory electron transport
Potential therapeutics for SARS
The citric acid (TCA) cycle and respiratory electron transport
Neuronal System
Transmission across Chemical Synapses
−0.2
0.0
0.2
0.4
0.6
Positive enrichment in cell lines
Negative enrichment in biopsies
Signaling by EGFR
NOTCH4 Activation and Transmission of Signal to the Nucleus
−0.4
−0.2
0.0
0.2
s dist
dataset
Biopsies
Cell lines
p.adjustMANOVA
0.05
0.04
0.03
0.02
0.01
0.00
setSize
10
50
100
500
1000